Final Report

Project Title: **RF Photonics for Phased-Arrays**

Contract number: **N00014-96-1-0799** (ONR Young Investigator Award)

Principal Investigator: **Dr. Robert York**

Period of Performance: 5/1/96 – 10/31/99

19991101 017

REPORT DOCUMENTATION PAGE

Public reporting burden for this collection of information is estimated to average 1 hour per response, including the time for reviewing instructions, searching existing data sources, gathering and maintaining the data needed, and completing and reviewing the collection of information. Send comments regarding this burden estimate or any other aspect of this collection of information, including suggestions for reducing this burden, to Washington Headquarters Services, Directorate for Information Operations and Reports, 1215 Jefferson Davis Highway, Suite 1204, Arlington, VA 22202-4302, and to the Office of Management and Budget, Paperwork Reduction Project (0704-0188), Washington, DC 20503.

1. AGENCY USE ONLY (Leave Blank)	2. REPORT DATE 25 October 99	3. REPORT TYPE AND DATES COVERED Final Technical Report 1 May 96 to 31 October 99	
4. TITLE AND SUBTITLE RF Photonics for Phased-Arrays		5. FUNDING NUMBERS N00014-96-1-0799	
6. AUTHORS Robert A. York			
7. PERFORMING ORGANIZATION NAME(S) AND ADDRESS(ES) Department of Electrical and Computer Engineering University of California, Santa Barbara Santa Barbara, CA 93106-9560		8. PERFORMING ORGANIZATION REPORT NUMBER	
9. SPONSORING / MONITORING AGENCY NAME(S) AND ADDRESS(ES) Office of Naval Research 800 North Quincy Street Arlington, VA 22217--5660		10. SPONSORING / MONITORING AGENCY REPORT NUMBER	

11. SUPPLEMENTARY NOTES

12a. DISTRIBUTION / AVAILABILITY STATEMENT Approved for public release; distribution unlimited	12b. DISTRIBUTION CODE

13. ABSTRACT (Maximum 200 words)

The initial goals of this project were to examine and develop practical photonic technologies suitable for shared-aperture phased-array environments. This effort resulted in an integrated optically-variable capacitor (OVC) technology which can be implemented in a variety of RF circuit and radiating structures for optical control. This technology was developed using monolithic GaAs-based photovoltaic devices and varactors developed at UCSB. A novel integration scheme and circuit were successfully developed and demonstrated in several RF circuits (tunable filters and phase shifters) and antennas (planar folded-slot structures). An especially attractive feature of the technology is the extremely low optical power requirement; the tunable circuits were all controlled with less then 1 mW of optical power, in some cases less than 500µW. In addition, the indirect nature of the optical control allows for the independent development and optimization of the optical and RF circuits, allowing for improved performance in both the optical and RF regimes, and also making the technology amenable to retrofitting. The resulting technology is well-suited to control of shared-aperture systems where the attractive features of optical control (light weight, low transmission loss, high speed, high isolation, microwave transparency, and immunity to EMI) are required.

14. SUBJECT TERMS Photonics, Photovoltaics, Varactors, Microwave Circuits, Antennas	15. NUMBER OF PAGES 72
	16. PRICE CODE

17. SECURITY CLASSIFICATION OF REPORT Unclassified	18. SECURITY CLASSIFICATION OF THIS PAGE Unclassified	19. SECURITY CLASSIFICATION OF ABSTRACT Unclassified	20. LIMITATION OF ABSTRACT UL

Table of Contents

Project Summary

The initial goals of this project were to examine and develop practical photonic technologies suitable for shared-aperture phased-array environments. During the early stages of this program, a close partnership developed between UCSB and Toyon Research Corporation, a neighboring company with strong interests in this area and similar ties to Office of Naval Research funding. In consultation with the ONR program director (Dr. William Miceli), the focus of this project was shifted slightly to focus mostly on one of the two photonic technologies described in the original proposal, namely, indirect optical control of microwave circuits and antennas. This final report summarizes extensive work in this area, adapted from the PhD thesis of Dr. Amit Nagra, the primary recipient of support under this program.

This effort resulted in an integrated optically-variable capacitor (OVC) technology which can be implemented in a variety of RF circuit and radiating structures for optical control. This technology was developed using monolithic GaAs-based photovoltaic devices and varactors developed at UCSB. A novel integration scheme and circuit were successfully developed and demonstrated in several RF circuits (tunable filters and phase shifters) and antennas (planar folded-slot structures). An especially attractive feature of the technology is the extremely low optical power requirement; the tunable circuits were all controlled with less then 1 mW of optical power, in some cases less than 500μW. In addition, the indirect nature of the optical control allows for the independent development and optimization of the optical and RF circuits, allowing for improved performance in both the optical and RF regimes, and also making the technology amenable to retrofitting. The resulting technology is well-suited to control of shared-aperture systems where the attractive features of optical control (light weight, low transmission loss, high speed, high isolation, microwave transparency, and immunity to EMI) are required.

Finally, this research led directly to the concept of a new beam-scanning technology using a distributed traveling-wave antenna with embedded variable reactances, and this is currently under development at UCSB under subcontract to Toyon Research Corp.

Publications and Theses:

The following publications and theses are directly attributed to funding under this program:

- Nagra and R.A. York, "FDTD Analysis of Wave Propagation in Nonlinear Absorbing and Gain Media", *IEEE Trans. Antennas & Prop.* , vol. 36, pp. 334-340, March 1998.

- T.L. Larry, A.S. Nagra, M.L. Van Blaricum, and R.A. York, "Photonic reconfiguration of Antennas using Reactive Control", *1998 Antenna Applications Symposium*, Allerton Park, Monticello, Illinois, September 1998.

- A.S. Nagra, P. Charvarkar, C.J. Swann, T.Larry, M.L. Van Blaricum, U.K. Mishra, and R.A. York, "Monolithic optically Variable Capacitors for Tunable Microwave Antennas", *16th biennial IEEE/Cornell University conference on Advanced Concepts in High-Speed Semiconductor Devices and Circuits* , (Ithaca, NY), pp.69-78, August 1997.

- R.A. York and T. Itoh, "Injection- and Phase-Locking Techniques for Beam Control", (Invited Paper), *IEEE Trans. Microwave Theory Tech.* , vol. 46, pp. 1920-1929, November 1998.

- A.S. Nagra, M.L. Van Blaricum, and R.A. York, "Low-Power Indirect Optical Reactance Control using Monolithic GaAs OVC™ Technology", *DARPA Photonic Systems for Antenna Applications Conference (PSAA)*, Monterey, CA 1998.

- A. Borgioli, A.S. Nagra, and R.A. York, "Reactively Loaded Antenna Arrays", *1999 IEEE AP-S/URSI International Symposium*, 1999.

- M.L. Van Blaricum, T.L. Larry, R.A. York, and A.S. Nagra, "Optical Reconfiguration of Antenna Elements and Feeds Using Reactive Control", *Workshop: Novel Approaches to Photonic-Antenna integration* , at 1998 IEEE MTT-S International Microwave Symposium (Baltimore).

- A.S. Nagra, O. Jerphagnon, P. Charvarkar, M. Van Blaricum, and R.A. York, "Indirect optical control of microwave circuits using monolithic optically variable capacitors", *IEEE Trans. Microwave Theory Tech.* , vol. MTT-47, pp. 1365–1372, July 1999

- Borgioli, A.S. Nagra, M.Van Blaricum, R.A. York, "Reactively Controlled Travelling-Wave Antenna Arrays", *to appear in IEEE Trans. Antennas and Propagation*, 2000.

- Amit S. Nagra, "Varactor based Technologies for the Tuning and Control of Microwave Circuits and Antennas" Department of Electrical and Computer Engineering, University of California at Santa Barbara, April 1999.

Technical Report

1. Optical Control of Microwave Circuits

The motivation for using optical signals for the control of microwave circuits and antennas is presented in this section. Microwave circuit and antenna applications that benefit from the use of optical control are listed. A brief survey of currently used optical control schemes is presented and the relative merits/demerits of the various schemes are discussed. This is followed by an introduction to the Optically Variable Capacitor (OVC), which has been employed by us for the optical control of microwave circuits and antennas. The basic principle of operation of the OVC, as well as the reasons for choosing the OVC for implementing optical control, are presented here.

1.1 Motivation for optical control

Optical control of microwave circuits and antennas is attractive for several reasons. One of the major advantages of optical control is that the control signal can be transmitted over optical fibers, as opposed to electronic control, where metallic wires/cables are required. Since optical fibers have low losses, they are suitable for the distribution of control signals over long distances, as is the case in large phased arrays and in remotely controlled antennas/circuits. Also, optical fibers are light (1/10 the weight of copper wire), compact, and flexible making them desirable for airborne and space applications where volume and weight savings are crucial. The wide bandwidth of optical fibers, along with the high-speed modulation capabilities of laser diodes/LEDs, makes optical control attractive for applications where high-speed control is required. Incidentally, due to the advantages discussed above, optical links are also being deployed in antenna feed networks for the distribution of the microwave signals. Thus the same fiber link can be used for the simultaneous distribution of the microwave signal (high frequency signal to be radiated) and the control signal (slower signal for controlling component performance).

The unidirectional nature of the optical to electrical conversion process provides extremely high isolation between the control circuit and the microwave circuit/antenna being controlled. This is especially important in high power applications where leakage through the control circuit can cause interference between the various components. The immunity of optical fibers to EMI (electromagnetic interference) makes optical control attractive for military applications. Also, optical fibers are virtually transparent to microwave signals since they are made of low permittivity dielectrics. This non-invasive nature of optical control makes it desirable in antenna applications where metallic wires/cables are undesirable because they perturb antenna radiation patterns.

Several microwave control applications benefit from using optical control. High speed switching and gating of microwave signals using photoconductive switches was amongst the first demonstrations [1] of optical control and considerable progress has been made in this field since then [2-4]. In addition to fast transient response, these optically controlled switches have the advantage of high power handling capability and picosecond timing precision. Another area where optical control has made significant impact is in the control of remotely located antennas or large phased arrays, where the control signal has to be sent over long distances. Optical control of the various components commonly employed in antenna

5

T/R modules such as attenuators [5, 6], amplifiers [7-9], tunable filters [10], switches [4, 11, 12], and phase shifters [5, 11, 13, 14] has been demonstrated. Significant contributions have also been made in optical control of oscillator circuits. Optical tuning of oscillation frequency [7, 15, 16], optical injection locking [7, 16] and optical control of oscillator phase [17, 18] have been demonstrated. Optical injection locking and phase control is attractive for large active antenna arrays used in power combining and beam steering applications.
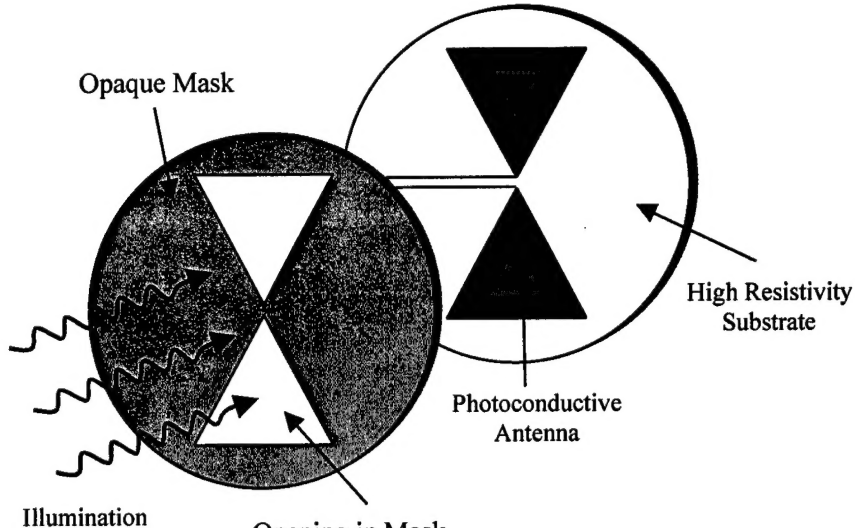

(a)
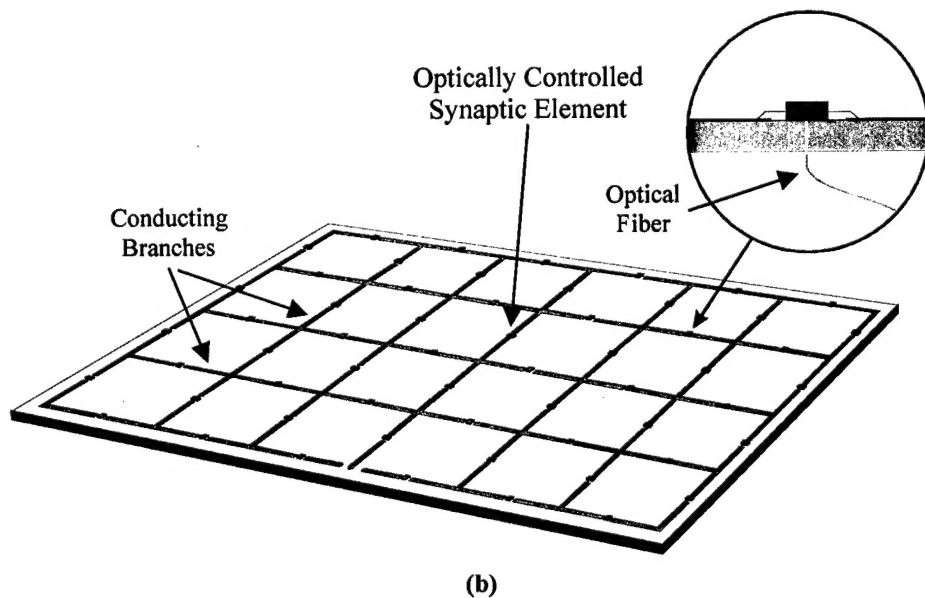
(b)

Figure 1.1: Schematic showing layout of a) Photoconductive antenna b) Optically reconfigurable synaptic antenna.

Another application where optical control has made major contributions is in reconfigurable antennas. There are two types of optically reconfigurable antennas: photo-conductive antennas, and synaptic antennas. Photoconductive antennas consist of selectively illuminated regions on a high resistivity semiconductor substrate.

A photoconductive bowtie antenna is depicted in fig. (1.1a). The illuminated regions, which are quasi-metallic in nature due to the high density of optically generated carriers, act as the radiating/receiving surfaces. By changing the mask pattern, photoconductive antennas of different shapes and having different properties can be optically generated. The disadvantage of this technique is that large optical powers (up to 50 W) are typically required for generating high carrier densities over the antenna surface. The other technique for implementing reconfigurable antennas is to have a grid of radiating sections interconnected by optically controlled synaptic elements (switches/reactive elements) as depicted in fig. (1.1b). By turning the switches on/off or by adjusting the reactive loading, the current path or the current amplitude/phase can be varied, thereby resulting in impedance tuning, beam/null steering and multi-frequency operation. Synaptic antennas are less versatile than photoconductive antennas since the underlying grid limits the possible antenna current distributions/shapes. However the synaptic approach requires much lower optical power since only a discrete number of elements are being controlled, as opposed to the illumination of large surfaces in the photoconducting antenna case. Note that since metallic control wires interfere with antenna radiation patterns, conventional electronic control of the synaptic elements is not feasible and hence optical control is required. Moreover, the optical control scheme used within the synaptic elements must not require DC bias (since bias supply to the elements would require the use of metal bias wires).

Optical Control of Microwave Components

Direct Control — Bulk Semiconductor, Junction Devices

Indirect Control — Photovoltaic Detectors, Biased Detectors
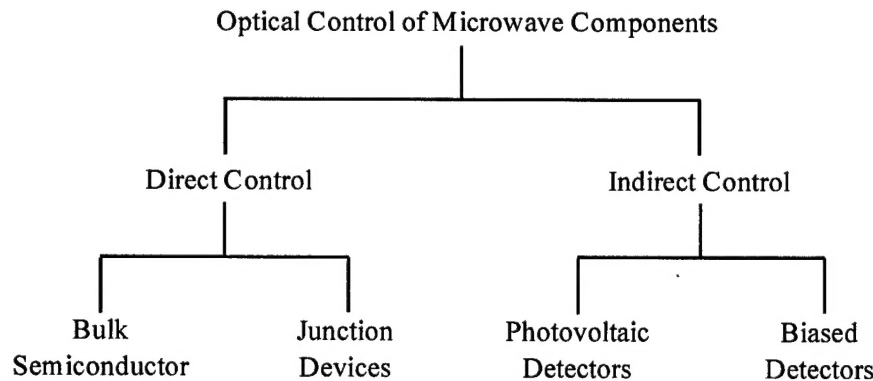
Figure 1.2: Classification table of the various optical control schemes

1.2 Comparison of optical control methods

Several different methods are being used for the optical control of microwave circuits and antennas. They can be broadly classified as direct and indirect control schemes. Direct optical control involves the illumination of the device being controlled. Here the same device performs both the optical and the microwave functions. Some direct optical control schemes rely on the illumination of bulk semiconductor substrates while others involve the illumination of semiconductor junction devices like

7

PIN diodes, FETs and Bipolar transistors. Indirect optical control involves the illumination of a dedicated optical detector that converts the optical control signal into a suitable electrical form, and controls the performance of a microwave device. Thus the optical and microwave functions are separated and performed by different devices. Depending on the photodetector bias conditions, indirect control schemes may be classified as photovoltaic control and control using biased detectors. Fig. (1.2) depicts the various optical control methods and how they are classified. The relative merits/demerits of these schemes are discussed in detail below.

Direct control using bulk semiconductor

This is the simplest of all optical control schemes and is also known as photoconductive control. It relies on the change in conductivity of semiconductor layers due to the photogeneration of carriers. For strong illumination intensities, the carrier density in the illuminated regions can be very high [1] and these regions then behave like degenerate plasmas with quasi-metallic properties. Fig. (1.3) illustrates a shunt CPW photoconductive switch fabricated on a bulk semiconductor substrate like high resistivity silicon/semi-insulating GaAs. In the absence of light, the microwave signal gets transmitted through the CPW structure with extremely small loss. However when the CPW gaps are illuminated, the photogenerated plasma creates an effective short circuit between the center conductor and ground causing most of the incident microwave signal to be reflected. Photoconductive conductive switches with up to 45 dB On/Off ratio have been demonstrated [4] but the optical power requirements are high (>100mW). In some applications like photoconductive antennas, where relatively large areas need to be illuminated, the optical power requirements can be as high as 50 W.
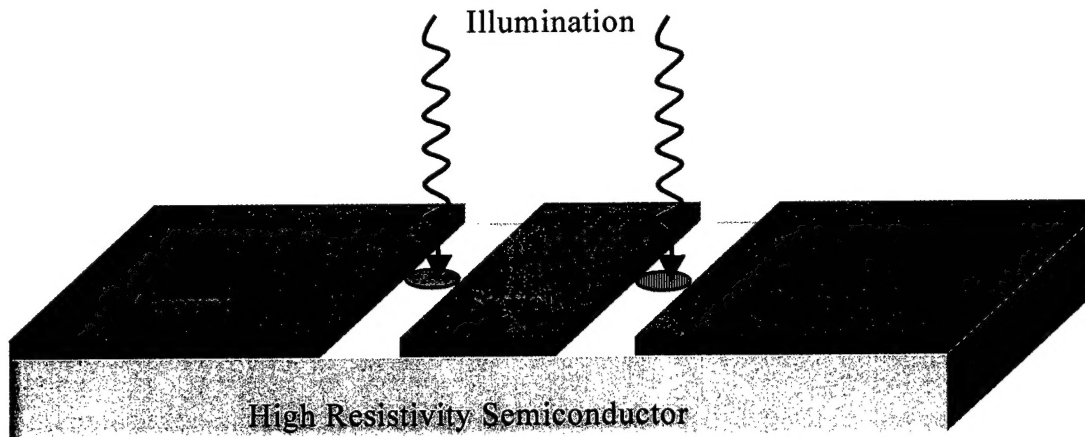

Figure 1.3: Shunt CPW photoconductive switch

Good performance of photoconductive devices relies on high carrier density, which is determined by illumination intensity and bulk carrier lifetimes in the substrate. Substrates with long carrier lifetimes, such as high resistivity silicon (τ >1µs), require considerably lower optical power than substrates like GaAs (τ ~1-5 ns) with short carrier lifetimes, but this decrease in power requirement comes at the cost of slower switching speeds. Thus there is a trade-off between optical power requirements and switching speed [4]. Note that photoconductive devices do not require any external DC bias. DC bias may be optionally used to sweep out the photogenerated carriers and increase the switching speed.

8

Direct control of junction devices

The effects of optical illumination on the DC and microwave performance of semiconductor junction devices have been extensively studied. Optical control of both two terminal devices like Gunn diodes, IMPATT diodes, PIN diodes [5, 16, 19, 20] and three terminal devices such as MESFETs, HEMTs and HBTs has been demonstrated [7, 8, 21].
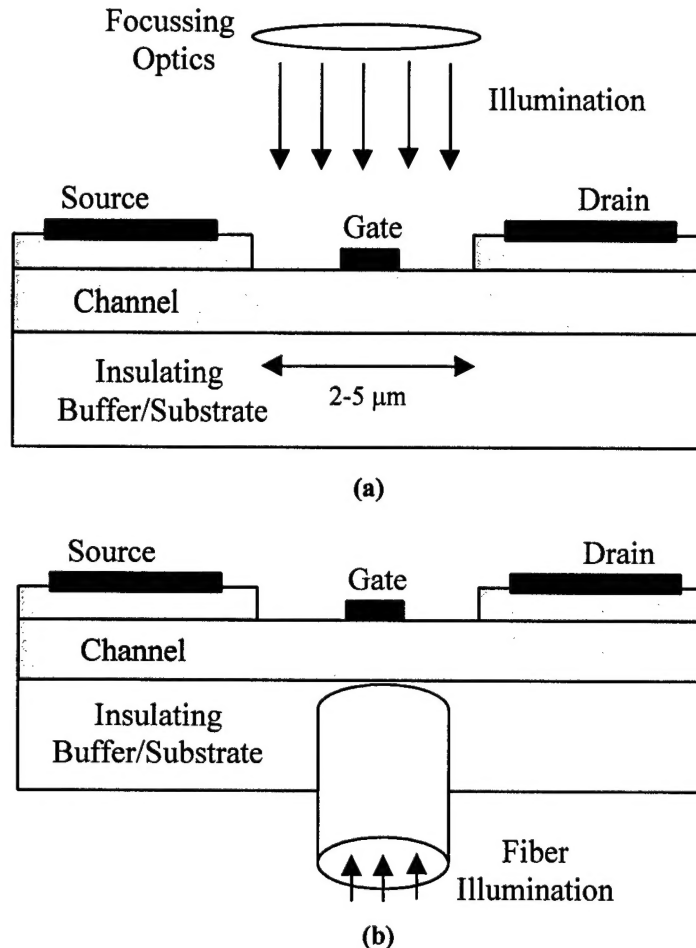

Figure 1.4: Illumination schemes for direct optical control of FETs.

Since FETs (both MESFETs and HEMTs) are the building blocks of MMICs and are widely used in microwave control circuits, most attention has been paid to the optical control of FETs. There are two physical mechanisms [7] responsible for the change in FET parameters under illumination- the photovoltaic effect (dominant) and the photoconductive effect (weak). To efficiently utilize the photovoltaic effect, the FET must be biased such that, in the absence of illumination, the channel underneath the gate is completely pinched off. When illuminated, the light induced voltage (photovoltaic effect in the gate Schottky diode) forward biases the gate and causing the drain current to increase. Under these bias conditions, the drain current is a strong function of illumination and the FET behaves like an optically controlled switch/amplifier. Note that in order for the photovoltaic effect to forward bias the gate, a sufficiently large gate bias resistor must be used. The switching speed is governed by the time

9

required to charge/discharge the gate capacitance through this gate bias resistor. The use of smaller resistors in the gate bias circuit can improve the switching speed the but at the cost of increased optical power to maintain the same switch performance [22]. Optically controlled switches with transient times of 1-10 µs have been demonstrated using commercial GaAs FETs. The switch transient times can be reduced to about 100 ns by improved FET design (small gate-source and gate-drain capacitance), more efficient light coupling, and by using the smallest gate bias resistor that allows adequate photovoltage to develop.

The photoconductive effect in the FETs is due to the presence of optically generated carriers in the channel/buffer/substrate that are swept across the gate and collected in the drain. The photoconductive effect is much smaller in magnitude compared to the photovoltaic effect (1-3 orders of magnitude smaller depending on bias conditions) but the speed of response [23] is much higher (50-100 ps). Due to the small change in FET drain current with illumination, this effect is useless for the optical control of FET switches and amplifiers. However it has been utilized for optical injection locking and synchronization of FET oscillators [7, 17].

One of the major drawbacks of direct optical control of FETs is the difficulty of effectively coupling light into the channel. Inefficient coupling of light into the active region is the reason why optical power requirements are moderately high (1-10 mW). FETs used in high frequency applications have small source-drain spacing (2-5 µm) and the alignment of light to the source-drain opening is critical. Also, as shown in fig. (1.4a), the gate tends to block some of the incident light. To avoid gate shadowing, the backside illumination scheme of fig. (1.4b) has been suggested [7] but the problem of small alignment tolerance still remains.

Indirect photovoltaic control

The basic principle of indirect photovoltaic control is illustrated in fig. (1.5). Here a photovoltaic (PV) array is used to convert the optical control signal into an electrical bias signal that varies the operating point of the microwave device/circuit. Since the PV array has no microwave requirements, its structure can be optimized for efficient coupling and absorption of light, thus reducing the optical power required. The indirect optical control of devices such as FETs [12, 24] and varactor diodes [25] has been successfully demonstrated using optical powers less than 1 mW.
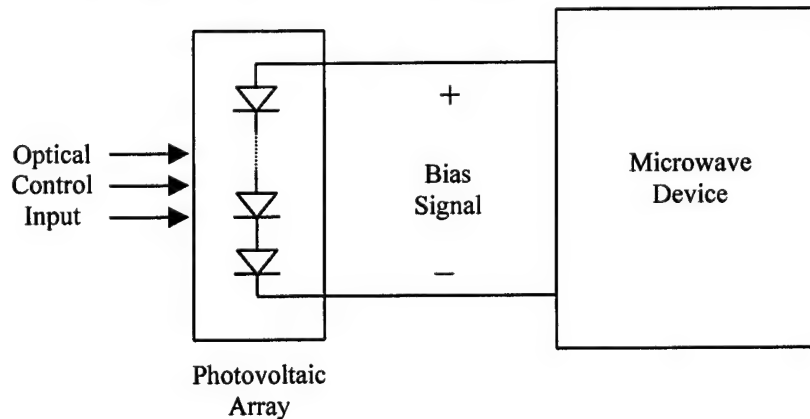

Figure 1.5: Indirect control using photovoltaic detectors

10

Apart from efficient utilization of optical power, another major feature of indirect control using PV arrays is that no external bias is required [12, 24]. This is a distinct advantage for antenna applications where metallic bias wires are undesirable as they interfere with radiation patterns. The switching speed of the photovoltaic approach is governed by the time required to charge/discharge the junction capacitance associated with the PV array. Transient times as small as 10 ns have already been demonstrated [24] and are sufficiently fast for most microwave applications.

Indirect control using biased detectors

This scheme basically employs an optical link [9, 13] instead of a metal wire to distribute the control signal. Electronic control information is used to modulate an optical signal, which is then launched onto an optical fiber. At the receiving end (shown in fig. (1.6)) a reverse biased photodetector (PIN diode/Schottky detector) is used to detect the optical signal and extract the electronic control information. The electronic control signal then goes through gain/level shifting blocks before being applied to the control input of a microwave circuit/system.

Note that this technique has subtle differences from the previously described photovoltaic control technique. Firstly, the photodetector used here is reverse biased for high-speed operation, as opposed to the photovoltaic scheme where the detector is unbiased. Also, in the previous scheme, the output from the photovoltaic array is providing bias to the device being controlled. In this scheme, the device being controlled needs an independent bias supply and the photodetector output just contains control information. Like in the photovoltaic control case, since an efficient photodetector is used for the optical to electronic conversion process, the optical power requirements are low. The speed of this scheme is basically just limited by the capability of the optical link. Fiber links with data rates of up to 40 Gbits/sec have been demonstrated and these are more than adequate for microwave control applications.
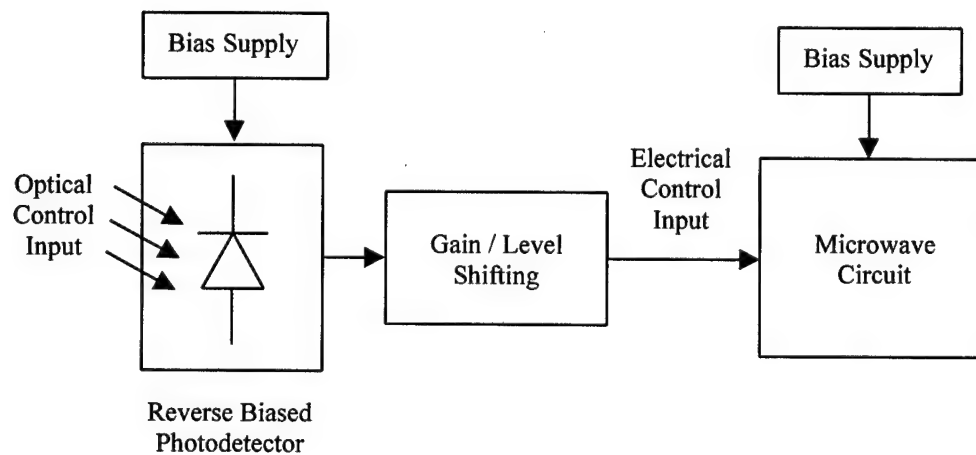

Figure 1.6: Indirect optical control using biased detectors

A brief summary of the underlying physical mechanisms, optical power requirements, bias requirements and switching speeds of the various optical control techniques is presented in table (1.1). It can be seen that the two indirect control schemes have the best performance in terms of low optical power

requirements and switching speed. This is due to the fact that the optical and microwave functions are performed in separate devices that can be independently optimized. Of the two indirect control schemes, only photovoltaic control is suitable for both antenna and circuit applications since it requires no external bias.

Control Technique	Mechanism	Optical Power Requirements	External Bias	Response Time
Direct illumination of bulk semiconductors	Photoconductive	High 0.1-100 W	Optional	Limited by carrier lifetimes in substrate (μs–ps)
Direct illumination of junction devices	Photovoltaic & Photoconductive	Moderate 1-10 mW	Required	Photovoltaic (>100 ns) Photoconductive (50-100 ps)
Indirect control using photovoltaic detectors	Photovoltaic	Low 0.1-1 mW	Not required	Limited by PV array junction capacitance (> 10 ns)
Indirect control using biased detectors	Photoconductive	Low 0.1-1 mW	Required	Limited by optical modulation and detection speeds (> 10 ps)

Table 1.1: Summary of properties of the various optical control schemes.

1.3 Introduction to the Optically Variable Capacitor (OVC)

As summarized above, photovoltaic control is the most effective scheme for the optical control of microwave antennas as well as circuits. Photovoltaic control of FETs for switching applications has been demonstrated in both hybrid [12] and monolithic form [24]. For applications that require optical control of reactive loads, an Optically Variable Capacitor (OVC) has been employed [25, 26]. The OVC relies on photovoltaic control of a Schottky varactor diode and is described in more detail in the following paragraphs.

The Optically Variable Capacitor (OVC) essentially consists of a photovoltaic array and a Schottky diode that are connected as shown in the circuit schematic in fig. (1.7a). The PV array generates a light dependent output voltage that reverse biases the Schottky diode and hence determines its depletion capacitance. Thus this arrangement allows the Schottky diode capacitance to be varied using an optical signal instead of the conventional electronic bias signal.

The OVC arrangement shown in fig. (1.7a) has several desirable features. The Schottky diode employed here is always reverse biased, hence it draws very little DC power from the bias supply. Since this bias is supplied by the PV array, the optical power requirements for the OVC are small. The separation of the optical and microwave functions allows the detector and varactor to be optimized independently of each other. The varactor diode is designed such that it is capable of the desired capacitance swing with the lowest possible RF insertion loss. The PV array is designed to generate the desired range of output voltages with the smallest amount of optical power. Ease of coupling light and efficient utilization of the incident optical power are the main concerns for the PV array. The RF blocking resistor shown in fig. (1.7a) is used to prevent the microwave signal from entering the PV array. This

12

ensures that the optical control components do not affect the microwave performance of the varactor diode. Hence it is possible to design the OVC such that there are no RF performance penalties for using optical control. The fixed DC load resistor shown in fig. (1.7a) serves two purposes-a) it enables better of control PV array output voltage under weak illumination conditions and b) it serves as discharge path for the PV array and helps improve the transient response.

The OVC configuration shown in fig. (1.7b) is a slight modification of the simple configuration discussed above. The main difference here is that the varactor diode is implemented in the form of two identical back to back Schottky diodes. The PV array is connected to the common terminal of the two diodes and it can be verified that the array output voltage reverse biases both diodes by the same amount. The RF blocking resistors and the fixed DC load resistor have the same functions as their counterparts in fig. (1.7a). The main benefit of this arrangement is that no DC voltage appears across the microwave terminals of the OVC. This is important for applications where several devices, each with independent bias settings, need to be connected in parallel. Also, the connection of capacitive loads across the microwave terminals does not affect the switching speed in this configuration.


(a)

(b)
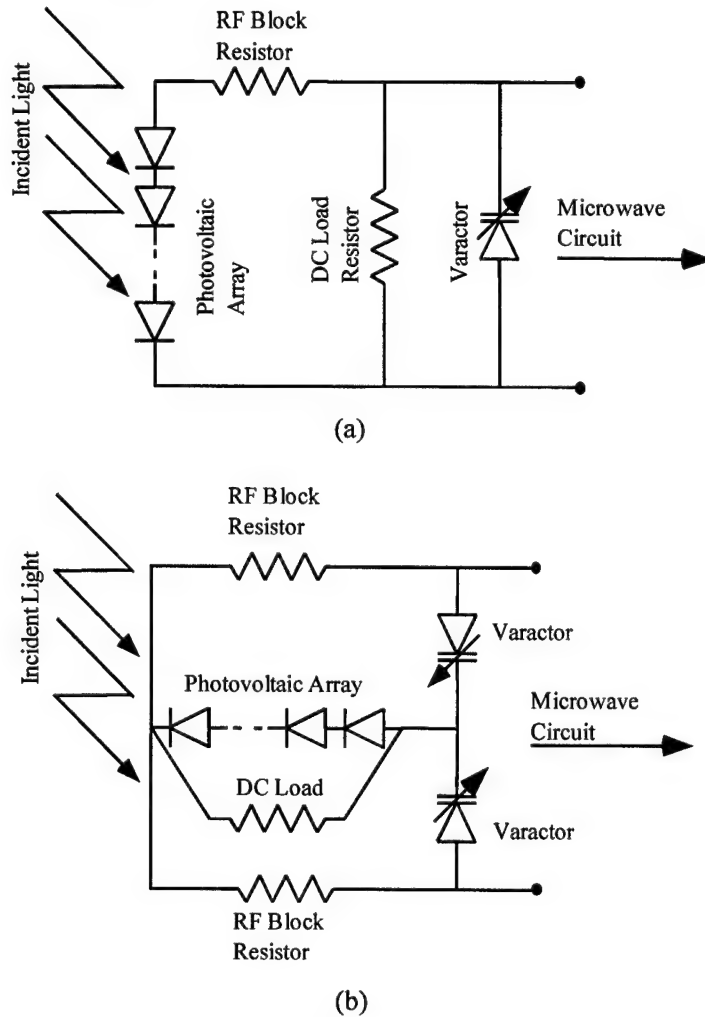
Figure 1.7: Circuit schematics for the Optically Variable Capacitor

13

1.4 Monolithic integrated OVC

A hybrid version of the OVC depicted in fig. (1.7), assembled from commercially available components, was used to demonstrate [27] optical tuning of a loop antenna at 1GHz. The large size (constrained by size of the PV array) and connection parasitics associated with the hybrid OVC limited its use to relatively low frequencies. For optical control of high frequency circuits/antennas, a monolithic version of the OVC has been developed [25, 26]. It integrates a miniature PV array with a varactor diode and bias resistor on the same chip. In addition to high frequency operation capability, the monolithic OVC also has superior switching speed compared to the hybrid version due to lower PV array capacitance.

The design and fabrication of the monolithic OVC posed several interesting challenges. The material system and the epitaxial layer structure had to be chosen such that both high frequency varactor diodes as well as efficient PV arrays could be fabricated on the same wafer. Conventional PV cells are vertical devices (require top and back contacts) with thick active regions for high conversion efficiency. However, this makes them unsuitable for monolithic integration, so planar PV cells had to be developed. Additionally, effective isolation schemes to prevent leakage between the various cells within a PV array were required. All these issues are addressed in greater detail in the next section.

References

[1]   A. M. Johnson and D. H. Auston, "Microwave switching by picosecond photoconductivity," *IEEE Journal of Quantum Electronics*, vol. 11,, pp. 283-2871975.

[2]   C. H. Lee, "Optical control of semiconductor closing and opening switches," *IEEE Transactions on Electron Devices*, vol. 37, pp. 2426-38, Dec. 1990.

[3]   W. Platte, "Optoelectronic microwave switching," *IEE Proceedings J Optoelectronics*, vol. 132, pp. 126-32, April. 1985.

[4]   S. E. Saddow and C. H. Lee, "Optical control of microwave-integrated circuits using high-speed GaAs and Si photoconductive switches," *IEEE Transactions on Microwave Theory and Techniques*, vol. 43, pp. 2414-20, Sept. 1995.

[5]   P. J. Stabile, A. Rosen, and P. R. Herczfeld, "Optically controlled lateral PIN diodes and microwave control circuits," *RCA Review*, vol. 47, pp. 443-56, Dec. 1986.

[6]   S. E. Saddow, B. J. Thedrez, and C. H. Lee, "An optoelectronic attenuator for the control of microwave circuits," *IEEE Microwave and Guided Wave Letters*, vol. 3, pp. 361-2, Oct. 1993.

[7]   A. A. A. De Salles, "Optical control of GaAs MESFET's," *IEEE Transactions on Microwave Theory and Techniques*, vol. MTT-31, pp. 812-20, Oct. 1983.

[8]   R. N. Simons, "Microwave performance of an optically controlled AlGaAs/GaAs high electron mobility transistor and GaAs MESFET," *IEEE Trans. Microw. Theory Tech.*, vol. MTT-35, pp. 1444-551987.

[9]   P. R. Herczfeld and A. Paolella, "Optical gain control of a GaAs MMIC transmit-receive module compatible with optical spatial filters," in *IEEE Antennas and Propagation Society International Symposium Digest*, Syracuse, NY, USA, 1988, , pp. 40-3.

[10]   Y. Yamamoto, K. Kawasaki, and T. Itoh, "Optical control of microwave active band-pass filter using MESFETs," in *1991 IEEE MTT-S International Microwave Symposium Digest 91CH2870-4*, Boston, MA, USA, 1991, , pp. 655-8.

[11]   S. J. Rossek and C. E. Free, "Optically controlled microwave switching and phase shifting using GaAs FET's," *IEEE Microwave and Guided Wave Letters*, vol. 5, pp. 81-3, March. 1995.

[12]   C. K. Sun, R. Nguyen, C. T. Chang, and D. J. Albares, "Photovoltaic-FET for optoelectronic RF/ mu wave switching," *IEEE Transactions on Microwave Theory and Techniques*, vol. 44, pp. 1747-50, Oct. 1996.

[13]   K. B. Bhasin, P. C. Claspy, M. A. Richard, R. R. Romanofsky, M. Bendett, G. Gustafson, and W. Walters, "Control of a GaAs monolithic Ka-band phase shifter using a high-speed optical interconnect," *IEEE Transactions on Microwave Theory and Techniques*, vol. 38, pp. 686-8, May. 1990.

[14]   P. Cheung, D. P. Neikirk, and T. Itoh, "Optically controlled coplanar waveguide phase shifters," *IEEE Transactions on Microwave Theory and Techniques*, vol. 38, pp. 586-95, May. 1990.

[15]   H. Hayashi, M. Nakatsugawa, T. Nakagawa, and M. Muraguchi, "A novel optical control technique using tunable inductance circuits," *IEICE Transactions on Electronics*, vol. E81-C, pp. 299-304, Feb. 1998.

[16]   A. J. Seeds, J. F. Singleton, S. P. Brunt, and J. R. Forrest, "The optical control of IMPATT oscillators," *Journal of Lightwave Technology*, vol. LT-5, pp. 403-11, March. 1987.

[17]   R. D. Esman, L. Goldberg, and J. F. Weller, "Optical phase control of an optically injection-locked FET microwave oscillator," *IEEE Transactions on Microwave Theory and Techniques*, vol. 37, pp. 1512-18, Oct. 1989.

[18]   A. S. Daryoush, "Optical synchronization of millimeter-wave oscillators for distributed architecture," *IEEE Transactions on Microwave Theory and Techniques*, vol. 38, pp. 467-76, May. 1990.

[19]   W. H. Haydl and R. Solomon, "The effect of illumination on Gunn oscillations in epitaxial GaAs," *IEEE Transactions on Electron Devices*, vol. Ed-15, pp. 941-2, Nov. 1968.

[20]   H. P. Vyas, R. J. Gutmann, and J. M. Borrego, "Leakage current enhancement in IMPATT oscillators by photoexcitation," *Electronics Letters*, vol. 13, pp. 189-90, March. 1977.

[21]   P. Freeman, Z. Xiangkun, I. Vurgaftman, J. Singh, and P. Bhattacharya, "Optical control of 14 GHz MMIC oscillators based on InAlAs/InGaAs HBTs with monolithically integrated optical waveguides," *IEEE Transactions on Electron Devices*, vol. 43, pp. 373-9, March. 1996.

[22]   A. Madjar, A. Paolella, and P. R. Herczfeld, "Modeling the optical switching of MESFET's considering the external and internal photovoltaic effects," *IEEE Transactions on Microwave Theory and Techniques*, vol. 42, pp. 62-71994.

[23]   L. E. M. de Barros, Jr., A. Paolella, M. Y. Frankel, M. J. Romero, P. R. Herczfeld, and A. Madjar, "Photoresponse of microwave transistors to high-frequency modulated lightwave carrier signal," *IEEE Transactions on Microwave Theory and Techniques*, vol. 45, pp. 1368-741997.

[24]   J. L. Freeman, S. Ray, D. L. West, and A. G. Thompson, "Optoelectronic devices for unbiased microwave switching," in *1992 IEEE MTT-S International Microwave Symposium Digest Cat. No.92CH3141-9*, Albuquerque, NM, USA, 1992, , pp. 673-6.

[25]   A. S. Nagra, O. Jerphagnon, P. C. Chavarkar, M. L. VanBlaricum, and R. A. York, "Indirect control of Microwave circuits using low optical power," *IEEE Transactions on Microwave Theory and Techniques* 1999.

[26]   A. S. Nagra, P. Chavarkar, C. J. Swann, T. Larry, M. L. VanBlaricum, U. K. Mishra, and R. A. York, "Monolithic optically variable capacitors for tunable microwave antennas," in *Proceedings. IEEE/Cornell Conference on Advanced Concepts in High Speed Semiconductor Devices and Circuits*, Ithaca, NY, USA, 1997, , pp. 69-78.

[27]   M. L. VanBlaricum, C. J. Swann, and T. L. Larry, "Remote optical control and tuning of antenna elements," in *URSI Digest*, Newport Beach, CA, 1995, , pp. 18-23.

Varactor Diodes and Photovoltaic Arrays for the Monolithic GaAs OVC

This section deals with the two main components of the monolithic GaAs OVC- varactor diodes and photovoltaic (PV) arrays fabricated on GaAs. The motivation behind the fabrication of the monolithic OVC on GaAs is presented first. This is followed by details regarding the design of high-Q planar Schottky varactor diodes and high efficiency PV arrays on the same GaAs wafer. The challenges involved in integrating the epitaxial layer structures of the two devices and developing a compatible fabrication sequence are discussed. Conventional photovoltaic devices used in solar cell applications are vertical devices with thick active regions and they require front as well as back contacts. This makes integration using monolithic techniques very hard, so planar PV cells with limited active layer thickness and both contacts accessible from the front side were developed. These planar PV cells were integrated into monolithic PV arrays using airbridges for interconnections and a novel buried oxide isolation scheme was used for eliminating the problem of substrate leakage. Schottky diodes with a Q-factor of 40 at 10 GHz, and PV arrays with output voltages of 10.5 V and conversion efficiencies as high as 26.8% have been demonstrated on the same GaAs wafer, and the detailed results are presented here.

2.1 Choice of material system

There are several material systems in which the monolithic OVC could be implemented, such as silicon (Si), gallium arsenide (GaAs) and indium phosphide (InP). The need for a high resistivity substrate, on which the passive microwave components could be fabricated, favored the use of GaAs or InP since microwave losses on Si substrates are high. Also, due to lower electron mobilities in silicon, varactor diodes fabricated on silicon have lower cutoff frequencies than varactor diodes fabricated on GaAs or InP. Another factor against silicon was the fact that it is an indirect bandgap material and hence has a small optical absorption coefficient in the vicinity of its band edge. Thus the active layer in Si photodetectors has to be very thick for efficient absorption of the incident optical power. Both GaAs and InP are direct band gap materials with absorption coefficients that increase very rapidly near the band edge, thus making them suitable for optical detection applications where the active layer thickness is limited. Also, the larger bandgap of GaAs (E_g=1.4 eV) and InP (E_g=1.35 eV) result in photovoltaic detectors with larger open circuit voltages as compared to Si (E_g=1.1eV) photovoltaic detectors.

Thus, both GaAs and InP have considerable advantages over Si for the monolithic OVC application. Of these two, GaAs was chosen for several reasons- a) low-field electron mobilities in GaAs are higher than in InP, therefore GaAs varactor diodes have higher cutoff frequencies. b) GaAs based device technology is cheaper and more mature than InP technology. c) Since most commercially available MMICs are implemented using GaAs, the fabrication of the monolithic OVC on GaAs opens up the possibility of integrating the OVC with these MMICs.

2.2 Design of planar GaAs Varactor diodes

Schottky diodes fabricated on GaAs are employed as varactor diodes in a variety of applications [1] at microwave and millimeter wave frequencies. Although both PN junction diodes and Schottky diodes can be used as voltage variable capacitors, Schottky diodes are preferred in high frequency/low

loss applications because they are associated with lower series resistance. Series resistance associated with varactor diodes is the main source of loss at microwave frequencies and limits the useful frequency range of the device. One figure of merit commonly used for varactor diodes is the small signal cutoff frequency (f_c) that is defined as

$$f_c = \frac{1}{2\pi R_s C}$$

(2.1)

where R_s is the series resistance and C is the depletion capacitance associated with the varactor diode. The quality factor (Q) of the device at any frequency f can be expressed in terms of the small signal cutoff frequency as

$$Q = \frac{1}{2\pi f R_s C} = \frac{f_c}{f}$$

(2.2)
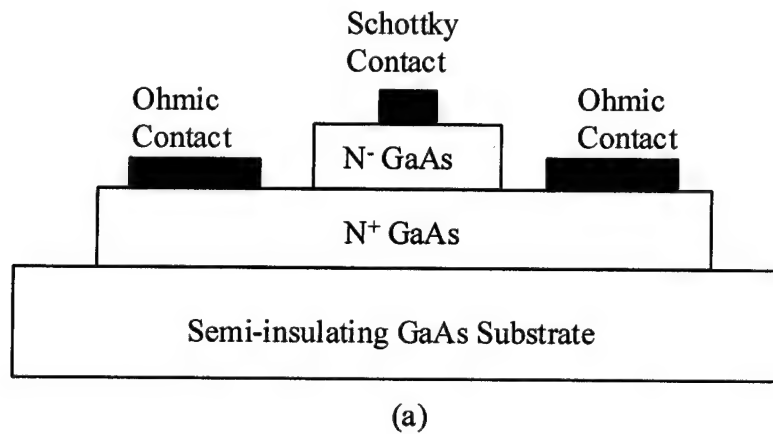
(a)
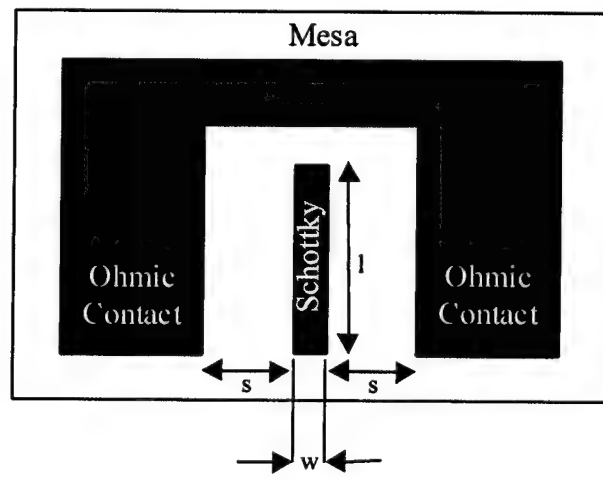
(b)

Figure 2.1: a) Cross section of a planar Schottky diode on n-type GaAs b) Layout of a planar Schottky diode

18

From equation (2.2) it can be easily seen the in order to obtain a high-Q varactor diode, the small signal cutoff frequency must be designed to be much higher than the frequency of interest.

Most high frequency applications employ planar varactor diodes because they are compact and can be easily integrated into circuits with minimal external parasitics. A planar varactor diode consist of a Schottky contact made on a N⁻ GaAs active region and recessed ohmic contacts to a heavily doped N⁺ GaAs layer as shown in fig. (2.1a,b). Each diode is fabricated on a separate mesa and the active region surrounding the mesa is etched down to the semi-insulating substrate for isolation. The capacitance of these diodes arises due to the space charge underneath the Schottky contact and is given by

$$C = \frac{\varepsilon A}{d} = wl\sqrt{\frac{qN_d\varepsilon}{(V_{bi} - V)}} \qquad (2.3)$$

where ε is the dielectric constant of GaAs, A is the area of the Schottky contact, w is the width of the Schottky stripe, l is the length of the Schottky stripe, d is the depletion width underneath the contact, q is the charge of an electron, N_d is the donor concentration in the N⁻ active region, V_{bi} is the built in voltage of the Schottky contact and V is the applied bias. From equation (2.3) it can be seen that depletion capacitance is a function of the applied reverse bias. As the reverse bias voltage applied to the Schottky diode is increased, the depletion width d increases causing the depletion capacitance C to decrease. Once the depletion edge has reached the N⁺ layer, it gets pinned and does not increase any further with increase in bias. In some cases if the N⁻ layer is too thick or the doping in the N⁻ is high, the Schottky diode may breakdown before the depletion edge reaches the N⁺ layer. Thus the thickness and doping of the N- layer determine the maximum capacitance swing that can be achieved. Note that for most applications, a capacitance ratio (C_{max}/C_{min}) of 3 is adequate and this requires a N⁻ thickness of the order of 0.3μm to 0.45μm depending on the doping. However the N⁻ layer is shared with the photovoltaic array (where it forms part of the optically active region) and so it must be thick enough (~ 1μm) to efficiently absorb the incident light. As a compromise, the N⁻ GaAs thickness used here is 0.7 μm. Since the purpose of the N+ GaAs layer is to reduce the series resistance, it is desirable to use the highest possible doping and the maximum thickness. The N+ doping in our diodes is limited by the ability of the MBE growth system at UCSB (~ 3 10¹⁸/cm³). The N⁺ layer thickness is constrained to 0.7 μm by the fact that the total epitaxial layer thickness has to be less than 2 μm of which 1.3 μm is taken up by the optically active layers required for the PV array. More details regarding the choice of layer thickness and the issues involved in integrating the epitaxial layers for the varactor with the PV array are discussed later.

With the thickness of the layers fixed by integration concerns, the only parameters needed to specify the design of the varactor diode are the active layer doping and the width and length of the Schottky contact. These parameters are chosen in a way to minimize the series resistance. As discussed in [2], the series resistance of these planar devices has contributions from the contact resistance (R_c) of the N-ohmic contacts, the resistance of the buried N+ layer (R_{N+}), the current spreading resistance (R_{spr}) and the resistance of the N- layer (R_{N-}).

$$R_s = R_c + R_{N+} + R_{spr} + R_{N-} \qquad (2.4a)$$

$$R_s = \frac{r_c}{2l} + \frac{d}{2l}\left(\frac{\rho^+}{t^+}\right) + \frac{w}{12l}\left(\frac{\rho^+}{t^+}\right) + \frac{\rho^- t^-}{wl} \qquad (2.4b)$$

where r_c is the contact resistance per unit width, ρ^+ and t^+ are the resistivity and thickness of the N^+ layer, and ρ^- and t^- are the resistivity and thickness of the N^- layer respectively. The width of the Schottky contact is w and the length is l as indicated in fig. (2.1b). Note that the first three terms are independent of area and depend solely on the periphery of the diode. Thus by lateral scaling i.e. reducing the width of the Schottky contact but keeping the area constant by increasing the length, it is possible to reduce the series resistance while maintaining a constant capacitance. Vertical scaling (increasing the active layer doping and reducing N^- thickness) becomes important when lateral scaling reduces the periphery dependant terms and the area dependant term R_{N^-} becomes dominant.

Fig. (2.2) shows the effect of Schottky contact width and active layer doping on the small signal cutoff frequency of the varactor diodes. These curves have been calculated using values appropriate to our device- r_c=0.08 Ω mm, ρ^+=3 10^{-3} Ω cm, t^+= 0.7 μm, t^-=0.7 μm and ρ^- estimated from active layer doping. A Schottky to ohmic spacing s of 4 μm is used for the curves in fig. (2.2) and the Schottky contact width w is varied from 1 μm to 4 μm. From these curves, it is apparent that the smallest possible Schottky contact width is desirable for high cutoff frequencies. However, due to device processing limitations, the minimum Schottky width employed in our varactor diodes is 2 μm. The mesa etching process introduces height variations on the surface of the GaAs wafer of the order of 2 μm (total epitaxial layer thickness) which requires the use of thick photoresist. This constrains the minimum feature size that can be accurately/reproducibly written using contact lithography to ~ 2 μm.
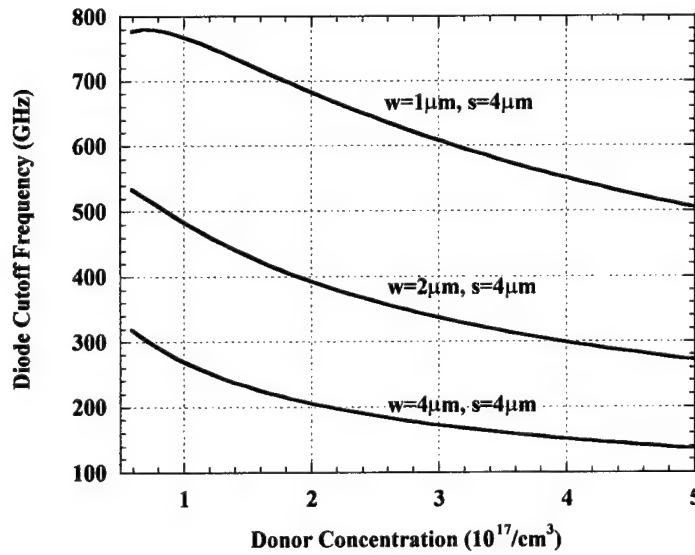

Figure 2.2: Varactor diode small signal cutoff frequency as a function of Schottky contact width and active layer doping

20

Another observation that can be made from fig. (2.2) is that the small signal cutoff frequency increases as the doping of the N⁻ layer is reduced. This is because lighter doped regions have smaller capacitance per unit area and so the periphery of a lightly doped diode has to be larger than that of a heavily doped diode for a given capacitance. Since in our diodes the periphery dependant terms are dominant, increased periphery leads to lower series resistance. Note that when the doping of the N- layer is made very small, the last term in equation (2.4) begins to dominate and this causes the series resistance to start increasing again. This can be seen in the flattening of the f_c versus N_d curves for very low doping. Accurate control of doping level is hard for doping densities below $1\ 10^{17}$/cm³ and dedicated doping calibration runs are required. Hence, a conservative value of $2\ 10^{17}$/cm³ was used as the doping density in the active N- region.

2.3 Fabrication and testing of Schottky Varactor diodes

A GaAs Schottky diode fabrication process was developed that was compatible with process used for fabricating the GaAs PV cells, since both components had to be integrated on the same wafer. The first step in the fabrication process was the definition of the diode mesa by RIE etching of GaAs using a $BCl_3/SiCl_4/Cl_2$ GaAs mixture. Next the p-type GaAs layer (part of the PV cell epitaxial structure) was etched away exposing the top of the active N⁻ GaAs layer. Ohmic contacts were formed by using a self aligned process to first etch down to the N⁺ contact layer and then depositing AuGe/Ni/Au contacts. The contacts were alloyed at 420°C for 1 minute and the measured contact resistance was about 0.08 Ω mm. Finally the Schottky contact to the N⁻ GaAs active layer was formed by depositing Ti/Pt/Au metal. Fig. (2.3) shows the process flow for the Schottky diode fabrication and details of the process are included in appendix A.

The Schottky diodes were connected to larger pads using airbridges for ease of DC and RF probing. The DC characterization of the Schottky diodes was carried out on a HP 4145 Semiconductor Parameter Analyzer. The I-V curve of a 2 μm x 40 μm Schottky diode under forward bias is presented in fig. (2.4a) and it can be seen that the Schottky diode turns on at a voltage of ~0.7 V. For higher forward bias voltages, the current is limited by the series resistance of the diode and probes. The series resistance of the Schottky diode was determined to be 2.65 Ω (after subtracting the 2.2 Ω contribution of the probes/measurement setup). Fig. (2.4b) depicts the Schottky diode forward current plotted on a logarithmic scale. The ideality factor (n) can be estimated from the slope of the I-V curves on the log scale (equation (2.5)) and was estimated to be 1.1 for our diodes.

$$n = \frac{16.7}{d\mathrm{Log}(I)/dV} \qquad (2.5)$$

The current versus voltage behavior under reverse bias is plotted in fig. (2.5) and it can be seen that the reverse breakdown voltage is ~ -7.5 V. Since the N- layer is thick in Schottky diode design used here, reverse breakdown occurs before the depletion edge gets pinned by the N+ layer. Thus the maximum capacitance swing in our diodes is limited by the reverse breakdown voltage and our calculations (equation (2.3)) indicate that a capacitance swing (C_{max}/C_{min}) of 3.1 is attainable before the diodes break down.

P GaAs
N⁻ GaAs
N⁺ GaAs
Semi-insulating GaAs Substrate

(a)

P GaAs
N⁻ GaAs
N⁺ GaAs

(b)

N⁻ GaAs
N⁺ GaAs

1.4 μm

(c)

Ohmic
Contact

Ohmic
Contact

N⁻ GaAs

N⁺ GaAs

(d)

Schottky
Contact

Ohmic
Contact

Ohmic
Contact
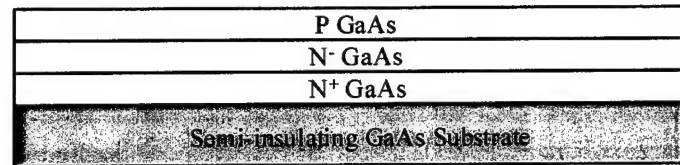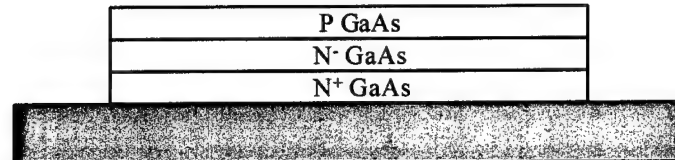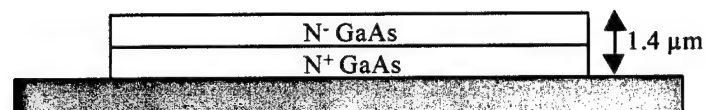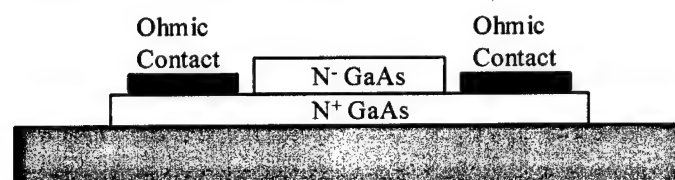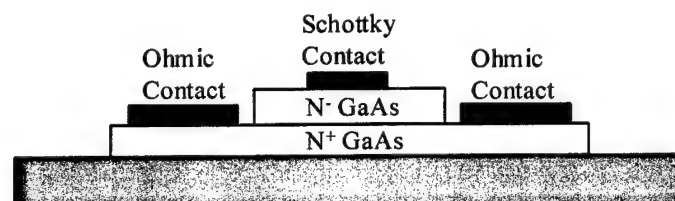
N⁻ GaAs

N⁺ GaAs

(e)

Figure 2.3: Fabrication process for the planar GaAs Schottky diodes

22
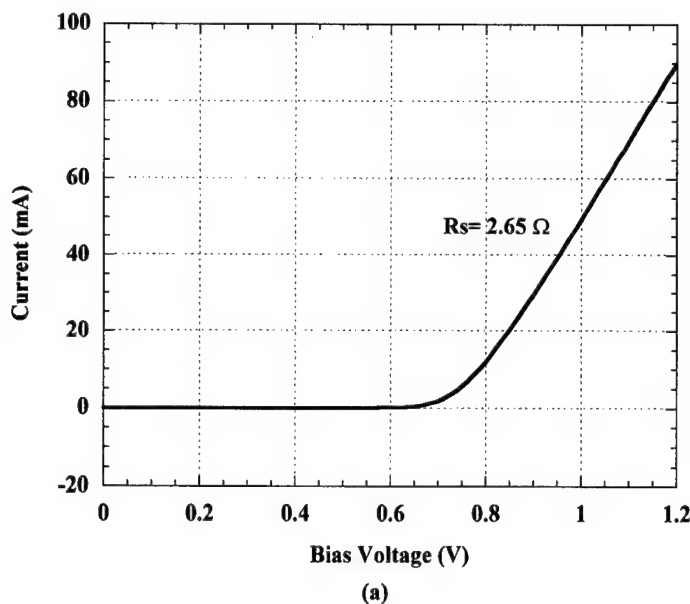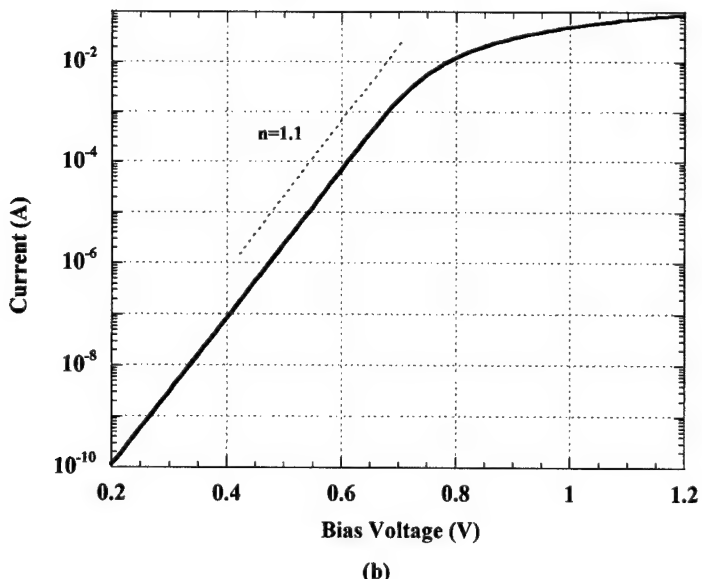
Figure 2.4: Forward I-V curves of a 2 μm x 40 μm planar Schottky diode on a linear scale (a) and logarithmic scale (b).

23
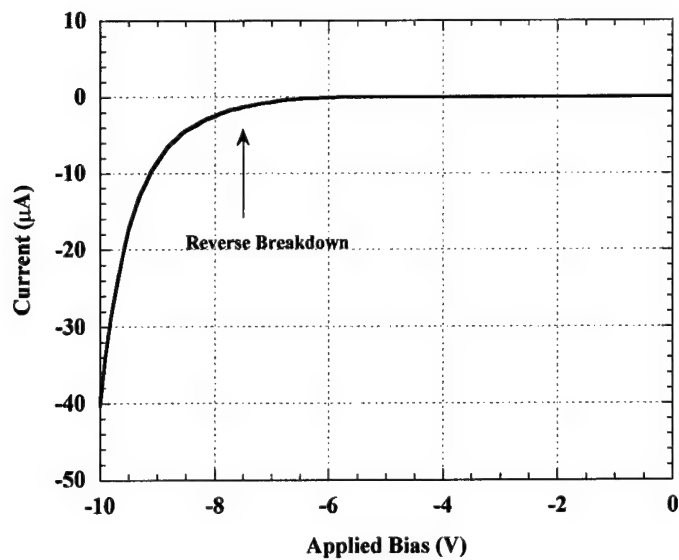
Figure 2.5: Reverse breakdown for planar Schottky diode on GaAs.
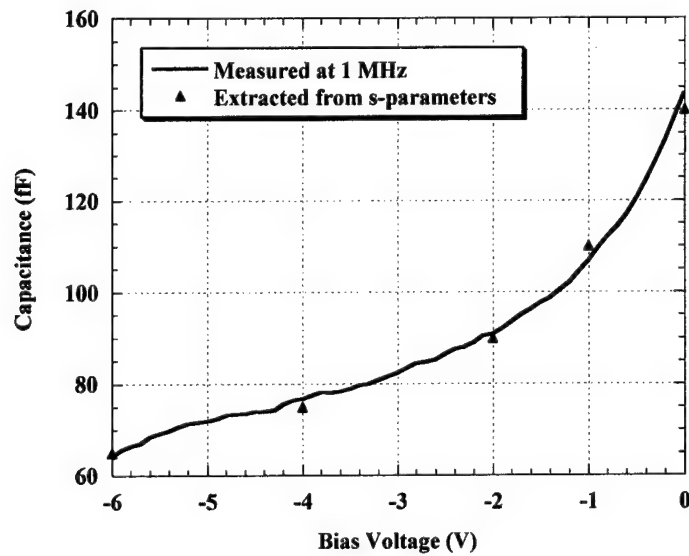
Figure 2.6: Comparison of capacitance versus voltage behavior measured at 1MHz and at high frequencies.

The capacitance versus voltage behavior of the Schottky diodes was characterized both at low frequencies (1 MHz) and in the frequency band of interest (0.5-18 GHz). At 1 MHz, direct C-V measurements were made using a Keithley 590 CV meter. The measured capacitance was corrected for parasitic pad capacitance and the results are plotted in fig. (2.6). A capacitance variation from 143 fF (0 V) to 65 fF (-6 V) was observed with bias, which corresponds to a capacitance ratio of 2.2.

The high frequency behavior of the diodes was studied by recording the 1-port s-parameters of the diodes for several values of reverse applied bias. The microwave s-parameters measurements were made on a Cascade Microtech probe station using ACP-40 CPW probes that were connected to a HP 8510 network analyzer. In order to de-embed the Schottky diode from the pads, an on-wafer reference standard comprising of probe pads terminated with a short circuit was used to set the reference plane at the position of the Schottky diode. The measured s-parameters were converted to equivalent admittance (Y) parameters and fitted to a simple series RC model using the method described in [3]. The real and imaginary part of the admittance for a resistor and capacitance connected in series is given by equation (2.6a)

$$Y = \frac{\omega^2 C^2 R}{1 + \omega^2 C^2 R^2} + j \frac{\omega C}{1 + \omega^2 C^2 R^2} \qquad (2.6a)$$

$$f \ll f_c, \quad Y = \omega^2 C^2 R + j\omega C \qquad (2.6b)$$

For frequencies well below the diode small signal cutoff frequency, the admittance (Y) can be expressed in the simpler form of equation (2.6b) which indicates that the imaginary part of Y varies linearly with frequency while the real part varies as the square of the frequency. The measured and modeled admittance are shown in figure (2.7a,b) and are in good agreement with each other. Note that for frequencies higher than 15 GHz, the measured data starts to diverge from the simple series RC model due to the de-embedding process used here. The pads were treated as a 50 Ω line and only the phase delay due to the size pads was taken into account. A more accurate de-embedding technique is outlined in [2] and uses a short-circuited pad and an open-circuited pad to obtain an equivalent inductance and capacitance for the pad. Using this technique it has been shown [2] that the simple series RC model is accurate up to 40 GHz.
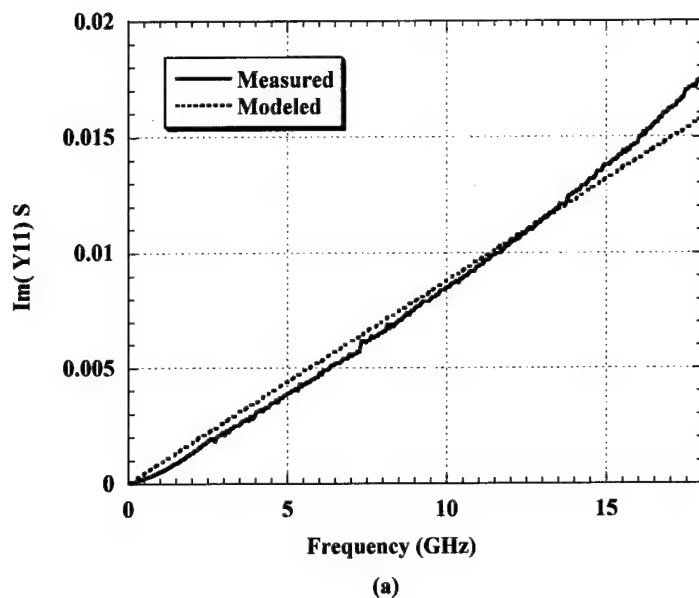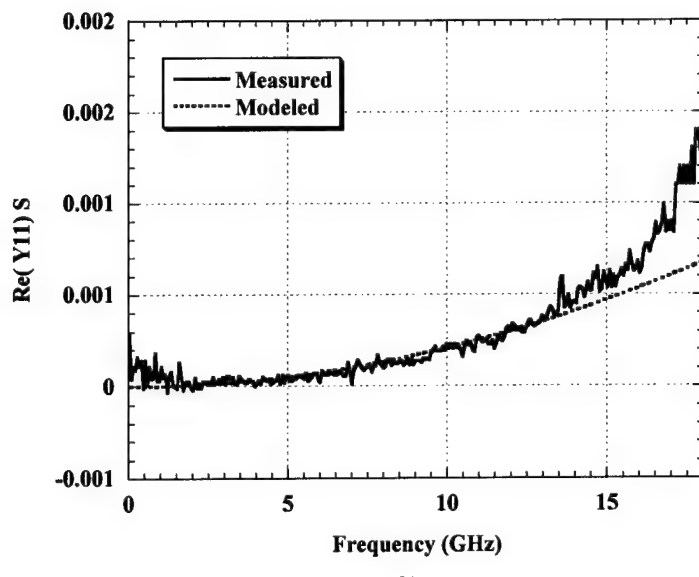
Figure 2.7: a) Comparison of the imaginary part of the measured and modeled admittance b) Comparison of the real part of the measured and modeled admittance.

The capacitance extracted from the high frequency s-parameters using the above mentioned technique compares well with values measured at 1 MHz as indicated in fig. (2.6). The series resistance of 2.87 Ω extracted from the high frequency data is only 8.4 % higher than the resistance value of 2.65 Ω estimated from the DC I-V curves. Using measured values for the capacitance and series resistance of the Schottky varactor diodes, the small signal cutoff frequency is calculated to be 390 GHz. Thus planar varactor diodes with a small signal cutoff frequency of 390 GHz and capacitance ratio of 2.2 have been demonstrated here. Moreover, these diodes are compatible with the epitaxial structure and fabrication process of the PV arrays required for the monolithic OVC.

2.4 Design of GaAs Photovoltaic detectors

Besides the varactor diode, the other major component of the OVC is the photovoltaic (PV) array, which converts the optical control signal into an electrical bias signal. The basic principle of operation of the photovoltaic detector employed here is similar to that of solar cells used for the generation of electrical power from solar radiation. However, as opposed to solar cells, which must efficiently absorb energy over a wide wavelength range (solar spectrum), the PV arrays employed in the OVC can be optimized to efficiently absorb optical energy in a narrow range of wavelengths since the illumination source is a laser diode/LED. This reduces the design complexity of the PV array. However, the integration of several photovoltaic detectors into a monolithic array, which is to be fabricated on the same wafer as high frequency varactor diodes, poses several constraints on the design of the monolithic PV array. All these design considerations are discussed in this section. As mentioned in section 2.1, the monolithic OVC is to be fabricated on GaAs; hence only GaAs based PV devices are considered here.
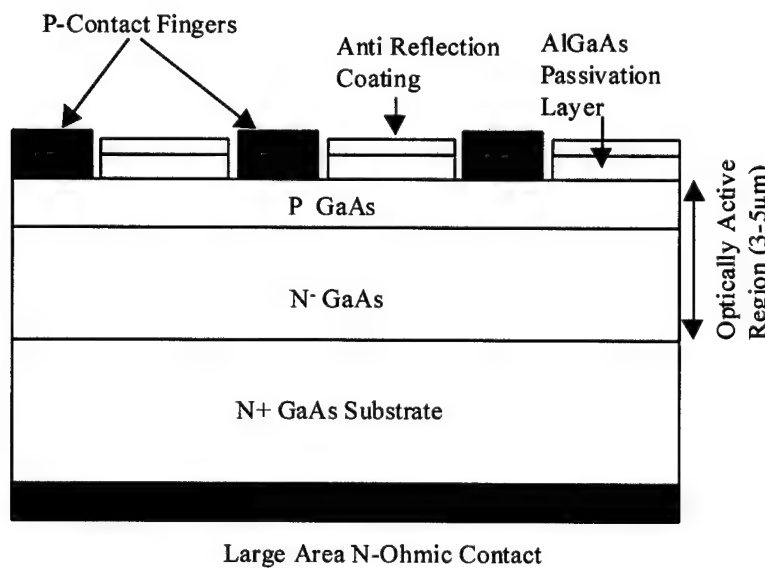

Figure 2.8: Cross section of a typical GaAs solar cell

Fig. (2.8) depicts the epitaxial structure and geometry of GaAs PV detectors used for solar cell applications [4-6]. The device shown here is a P-N homojunction diode although Schottky barrier diodes and heterojunction diodes can also be used as solar cells. The junction is relatively shallow (0.1-0.5μm)

27

and the active region is made thick (3-5μm) to efficiently absorb the incident optical energy. The top contact to the p-region is made in the form of narrow metal fingers to minimize the blocking of light. A large area back contact provides the ohmic contact to the n-region through the heavily doped substrate. An antireflection coating to minimize reflection of incident light at the air/GaAs interface and a passivation layer to reduce surface recombination velocity are applied at the top surface to increase cell efficiency.

(a)

(b)
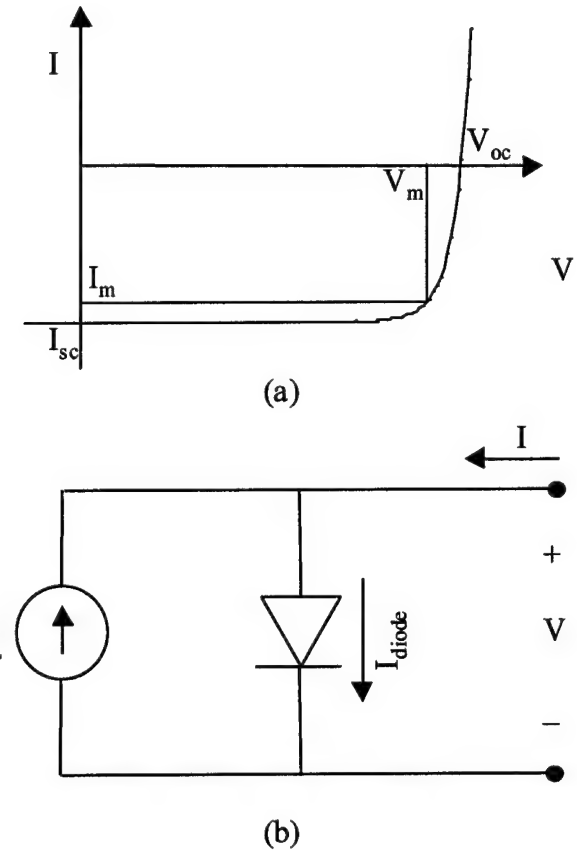
Figure 2.9: a) Typical I-V curve for a photovoltaic device under illumination b) Simple equivalent circuit for an illuminated PV device.

The bandgap of GaAs is 1.42 eV which corresponds to a threshold wavelength of 880 nm. When light with wavelength shorter than 880 nm is incident on the device, electron-hole pairs are generated, which increases the minority carrier concentrations in the device. The excess minority carriers (electrons in the p-region and holes in the n-region) that are able to diffuse to the junction before they recombine are swept across the junction by the built in field. The carriers generated within the depletion region are also swept across the junction by the built in field. This flux of optically generated carriers gives rise to a current that flows in the same direction as the reverse saturation current of the diode. The effect of illumination on the electrical characteristics of a diode is shown in fig. (2.9a). It can be seen that the light induced current opposes the forward current of the diode and translates the I-V curve downward into the fourth quadrant. Since the I-V curve passes through the fourth quadrant, it indicates that the device is

28

capable of delivering power to an external load. The equivalent circuit model for an illuminated diode is shown in fig. (2.9b) and consists of a current source, which accounts for the photocurrent, connected in shunt with an ideal diode.

The current versus voltage behavior of an illuminated diode can be described by the following equation

$$I = I_0\left(e^{\frac{qV}{nkT}} - 1\right) - I_{photo} \tag{2.6}$$

where the first term is the current of a diode in the absence of illumination and I_{photo} is the optically generated current. Note that the polarity of the photocurrent has been correctly chosen to oppose the forward current in the diode. Under short circuit conditions (V=0), the diode current goes to zero and it can be seen from equation (2.7) that the entire photocurrent is delivered to the short circuit.

$$V = 0 \quad \Rightarrow \quad I_{sc} = -I_{photo} \tag{2.7}$$

Under open circuit conditions (I=0), a positive voltage appears across the terminals of the diode. The physical basis for the open circuit voltage can be understood by balancing the drift and diffusion components of the diode current. Since the net current flowing out of the device terminals must be zero, the built in junction potential decreases (i.e. the diode develops a forward bias) so that the diffusion current component can cancel the light induced drift current.

$$I = 0 \quad \Rightarrow \quad I_0\left(e^{\frac{qV_{oc}}{nkT}} - 1\right) = I_{photo} \quad \Rightarrow \quad V_{oc} = \frac{nkT}{q}\ln\left(\frac{I_{photo}}{I_0} + 1\right) \tag{2.7}$$

The short circuit current and open circuit voltage points are indicated on the I-V curve depicted in fig. (2.9a). Also shown is the point at which maximum power is delivered to an external load. The maximum power is $P_m = V_m I_m$ and occurs when the load impedance R_l connected to the cell is given by

$$R_l = \frac{V_m}{I_m} \tag{2.8}$$

The power conversion efficiency η is the ratio of the maximum electrical power delivered to the load to the optical power incident on the device. Equation (2.9) expresses the power conversion efficiency in terms of the open circuit voltage, short circuit current, incident optical power P_{opt} and the fill factor FF. The fill factor depends on the shape of the I-V curve and is defined in equation (2.10).

$$\eta = \frac{V_m I_m}{P_{opt}} = \frac{FF\, V_{oc} I_{sc}}{P_{opt}} \tag{2.9}$$

$$FF = \frac{V_m I_m}{V_{oc} I_{sc}} \tag{2.10}$$

Thus in order to obtain the highest possible conversion efficiency, it is essential to maximize the short circuit current (I_{sc}), the open circuit voltage (V_{oc}) and the fill factor (FF). The following paragraphs outline how these terms can be increased by appropriate design of the PV cell.

As indicated in equation (2.7), the open circuit voltage (V_{oc}) varies as the logarithm of the ratio of the photocurrent to the reverse saturation current and hence the ratio I_{photo}/I_o should be made as large as possible. This requires that the incident light be absorbed efficiently to generate the maximum possible photocurrent. It is also desirable to have a low reverse saturation current I_o, which decreases exponentially with increasing bandgap. Thus all other factors being the same, diodes made from materials with a larger bandgap generate higher open circuit voltages. As discussed earlier, this is one of the advantages of using GaAs PV cells instead of silicon cells. Another important consideration in obtaining high open circuit voltages is that the ideality factor n of the diodes be as close to unity as possible. Although it appears from equation (2.7) that larger ideality factors ($n>1$) may enhance the open circuit voltage, in reality the opposite is true. Effects such as recombination within the depletion region, defect conduction, surface leakage along device periphery, which cause deviation from ideal diode behavior also cause the reverse current I_o to increase by several orders of magnitude. Thus although the ideality becomes larger ($n>1$), the ratio of I_{photo}/I_o decreases by several orders of magnitude so that the net effect is a smaller open circuit voltage.

The diode ideality factor n and open circuit voltage V_{oc} also affect the fill factor FF of the I-V curves. PV cells with higher V_{oc} have higher fill factors. For a given open circuit voltage, the fill factor increases as the diode ideality factor approaches unity. For example in GaAs PV cells operating at a V_{oc} of 0.9 V, the fill factor increases from 0.79 for $n=2$ to 0.87 for $n=1$. Two other factors that influence the fill factor are the series and shunt resistance of the cell. In order to obtain high fill factors, the series resistance must be small and the shunt resistance as large as possible.

There are several considerations that go into maximizing the photocurrent of PV cells. The thickness of the cell, carrier lifetimes in the active regions, and surface recombination velocity, all play a crucial role in determining how effectively the device converts the incident light into electrical current. A commonly used figure of merit is the quantum efficiency, which is a measure of the number of carriers collected at the terminals to the number of photons incident on the device, and is expressed as

$$QE = \frac{I_{photo}/q}{P_{opt}/h\nu} = \frac{I_{photo}}{P_{opt}} \frac{1.24}{\lambda(\mu m)} \qquad (2.11)$$

where I_{photo} is the photocurrent, P_{opt} is the optical power incident on the device, q is the charge of an electron, h is Planck's constant, ν is the frequency of the incident light and $\lambda(\mu m)$ is the wavelength in microns. Thus for a given optical power, the photocurrent is maximum when the quantum efficiency is maximum ($QE=1$). One of the key design rules for attaining high quantum efficiency is that the total depth of the active region must be large enough to absorb the incident light. Since the intensity of light falls off exponentially with depth ($e^{-\alpha x}$), it is sufficient to make the cell 3-4 times the absorption length ($1/\alpha$) to ensure that greater than 95% of the light is absorbed in the device. The absorption length (defined as the reciprocal of the absorption coefficient α) is a function of wavelength of the incident light. For GaAs, which is a direct bandgap semiconductor, the absorption coefficient increases rapidly just below threshold (from ~0 @880 nm to 1 10^4/cm @840 nm) and then increases slowly with decreasing wavelength (5 10^4/cm @600 nm). In order to be good energy conversion devices, GaAs solar cells are designed for efficient absorption of light over as wide a spectral range as possible. To ensure high quantum efficiency at the longer wavelengths (just below 880 nm) where the penetration depths are large, active layers with thickness in the range 3-5μm are commonly used in GaAs solar cells.

30

Recombination at the front surface of the cell as well as in the bulk material causes a reduction in the minority carriers available to be swept across the junction by the built-in fields. Thus in order to maximize the photocurrent, the loss of carriers to the competing mechanisms of surface and bulk recombination must be reduced as much as possible. Bulk recombination can be reduced by ensuring that lifetime of the minority carriers in the active regions is long resulting in large diffusion lengths. When the diffusion length of the minority carriers is large compared to the light penetration depth, a high percentage of the photogenerated carriers diffuse to the junction before they recombine and hence contribute to photocurrent. Although carrier lifetimes and diffusion lengths are not uniquely determined by the doping level (very sensitive to growth technique/growth conditions), they do increase when the doping is lowered. Thus lightly doped active regions are desirable for low bulk recombination losses. The effects of surface recombination, which occur due to the presence of surface states that trap the minority carriers, can be minimized by surface passivation layers. For GaAs the surface recombination velocity at the GaAs-air interface can be as high as 10^6 cm/sec. Several passivation layers have been explored for solar cell applications [7] but the most widely used is a thin layer of AlGaAs [6, 8] with high Al content (>80% Al). The low density of states at the AlGaAs-GaAs interface can reduce the surface recombination velocity by two orders of magnitude to about 10^4 cm/sec. The AlGaAs layer is made thin (0.03-0.1 μm) so that it absorbs an insignificant amount of the incident optical power at the shorter wavelengths.

Thus, the key requirements for high quantum efficiency in GaAs solar cells can be summed up as follows- a) active layers thick enough to absorb the longest wavelength of interest, b) lightly doped active regions with long minority carrier lifetimes and long diffusion lengths, and c) surface passivation with thin AlGaAs layers.
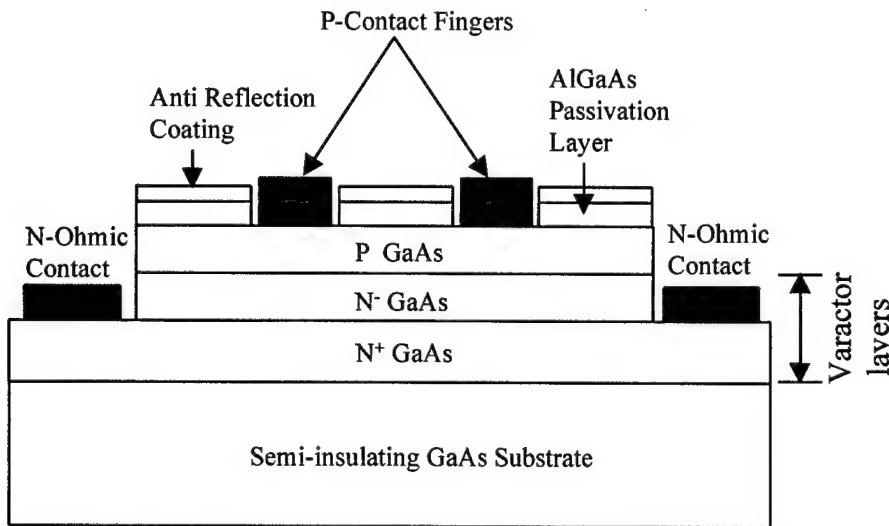

Figure 2.10: Cross section of a planar GaAs photovoltaic detector designed at UCSB for use in the monolithic OVC

The PV arrays used in the monolithic OVC differ from conventional GaAs solar cells in two aspects- 1) the PV cells are planar and 2) the active layer thickness is less than 2 μm due to fabrication and integration concerns. The vertical configuration employed in solar cells is not suitable for the OVC as it requires a heavily doped substrate (high microwave loss). Also, vertical cells require a bottom contact that makes monolithic integration a challenge. The planar PV cell configuration employed in the OVC is

31

depicted in figure (2.10). The cell is fabricated on a semi-insulating GaAs substrate. Contacts to both p-type and n-type regions are accessible from the front surface of the wafer thus making connections using monolithically fabricated airbridges easy. The airbridge process, which is employed to interconnect components within the OVC, requires that the total height variation on the GaAs wafer be no more than 2 μm. This limits the total epitaxial thickness of the OVC to 2μm . Another constraint on the PV array design is that the epitaxial layers must be shared with the varactor diode as both components are fabricated on the same wafer.

Due to the limited thickness of the active layer, the PV arrays employed in the OVC have low quantum efficiencies at longer wavelengths. However this is not a serious problem since the PV arrays used in the OVC do not need to cover a wide spectral range. In fact, the operating wavelength of the PV array is a design parameter. The PV arrays employed in the OVC are optimized for efficient operation in the 600-700 nm wavelength range. The main reasons for choosing this range of wavelengths is the availability of cheap illumination sources. The other reason is that the optical penetration depth in this range of wavelengths is well matched to the active layer thickness available in the OVC.

Details of a planar PV cell intended for use in the monolithic OVC are shown in fig (2.10). The top two layers (P^-GaAs and N^-GaAs) are the optically active layers while the bottom N^+ layer is the contact layer. The N^- GaAs and N^+ GaAs layers are shared with the varactor diode. The thickness h of the optically active region is chosen to be 1.3 μm as this corresponds to 3 absorption lengths ($1/\alpha$) at 700 nm, which is the longest wavelength of interest. Thus more than 95 % of the incident light is absorbed in the active region for all wavelengths less than 700 nm. The depth of the junction is chosen according to guidelines given in [4] where it is shown that for GaAs PV cells with passivation, the quantum efficiency is maximum when junction depth is around 0.6 μm. The doping in the P-type GaAs layer is 5 10^{17}/cm^3, which keeps the series resistance due to the P-type layer low while still maintaining long electron diffusion lengths. The doping used in the N^-GaAs layer is made low (2 10^{17}/cm^3) to ensure long hole lifetimes. Note that this low doping is also beneficial for the Schottky varactor diodes where the small signal cutoff frequency increases as the doping of the N^- GaAs layer is reduced. Since the total thickness of all the epitaxial layers can be at most 2 μm (of which the top 1.3 μm constitutes the optically active region), the bottom N+ layer is made 0.7 μm thick. This layer is doped heavily (3 10^{18}/cm^3) in order to lower the series resistance for the PV cells as well as the varactor diodes. A thin layer of Al$_{.85}$Ga$_{.15}$As is included on top of the P-type GaAs layer to reduce the recombination velocity at the front surface of the cell. An anti-reflection (AR) coating is also applied to the front surface of the cell to minimize reflection of light from the front interface. A silicon nitride film with refractive index 2.05 and thickness 100 nm is used as the AR coating here. Thus the epitaxial layers of the varactor diode and the PV array have been successfully combined in the design of fig. (2.10).

Fig. (2.11a) shows a theoretical spectral response curve (quantum efficiency versus wavelength) of the planar PV cell designed for the monolithic OVC. The spectral response curve is generated using a program which is described in appendix B. The program calculates the relative contributions of the P-layer, the N-layer and the diffusion region to the total photocurrent generated in the device and then estimates the quantum efficiency using equation (2.11). The values for the minority carrier lifetimes and diffusion lengths used in the program were taken from the literature for MBE grown material [8] with similar doping levels. Although the exact values of these parameters depend on growth conditions and processing steps, the values in appendix B provide a good starting point for verifying the design.

32
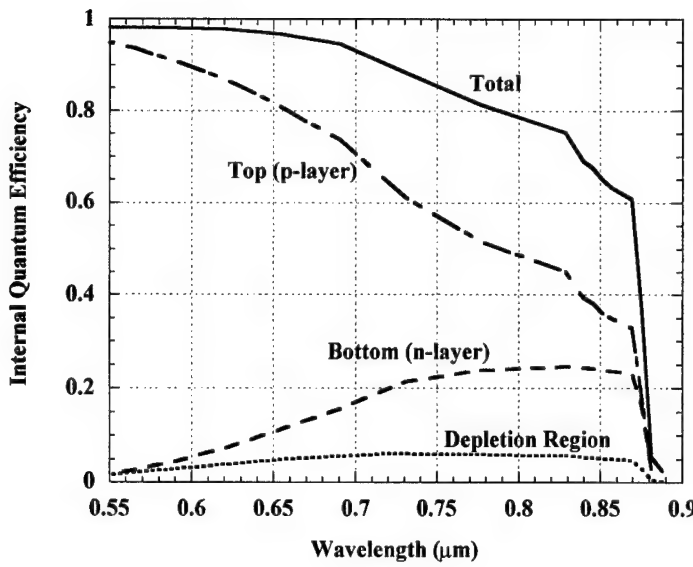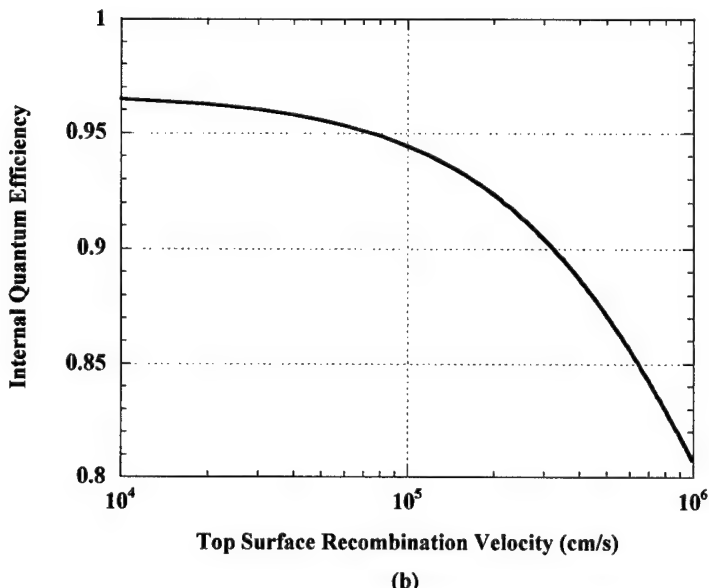
Figure 2.11: a) Simulated curve for quantum efficiency as a function of wavelength for a planar GaAs PV detector b) Simulated curve depicting effect of surface recombination velocity on the quantum efficiency at 670 nm.

The spectral response curve shows that for wavelengths longer than 700 nm the quantum efficiency is low due to the limited active layer thickness. However, in the wavelength range of interest (600-700 nm) the quantum efficiency is higher than 95%. It can also be seen that the major contribution to the photocurrent is from the top P-layer since most light is absorbed close to the front interface of the

33

cell. Thus, since a large number of carriers are generated close to the front surface, it is essential to reduce surface recombination velocity. Fig. (2.11b) shows the effect of front surface recombination velocity on the simulated quantum efficiency at a wavelength of 670 nm. It can be seen that the quantum efficiency drops from 97% to 81% when the recombination velocity increases from 10^4 cm/sec to 10^6 cm/sec. This reiterates the need for the AlGaAs passivation layer at the front interface.

2.5 Isolation and layout considerations

The photovoltaic detector used in the OVC must be capable of generating an output voltage greater than 7 V in order to obtain the full capacitance swing in the varactor diode. Since individual GaAs PV cells (PN junction type) have output voltages in the range 0.7-1.1 V, it was decided to use a PV array with 10 GaAs (PN junction) PV cells in series. In order for the PV array to work in the desired manner, it is essential that there be no leakage between the individual PV cells that are connected in an array. Parasitic leakage has deleterious effects on PV array performance as current can flow through the alternate leakage path instead of flowing through the series of PN junctions. This can lead to lower output voltages, smaller fill factors and lower energy conversion efficiency. Conventionally, devices fabricated on GaAs are isolated using mesa isolation. This involves etching away the active region surrounding each device to the semi-insulating substrate. However, mesa isolation by itself is not adequate [9, 10] to prevent leakage in monolithic PV array applications. Under illumination, a shunt leakage path exists between the devices due to photogenerated carriers in the semi-insulating substrate as depicted in fig. (2.12a). In order to prevent substrate leakage, an oxide layer is placed at the base of the individual device mesas as shown in fig (2.12b). This buried oxide layer is created by the lateral oxidation of $Al_{.98}Ga_{.02}As$ and serves to isolate the device from the photoconductive layer in the substrate. Since the oxide layer is insulating and its properties do not degrade under illumination, it provides an effective solution to the substrate leakage problem when used in conjunction with mesa isolation. A similar approach [11] has been used to reduce output conductance in GOI MESFETs and HEMTs due to buffer/substrate leakage.

The layout of the PV array requires careful consideration because it affects the energy conversion efficiency and the ease of coupling light into the array. As discussed in section 1, the monolithic PV array has to be small so that it can be embedded in high frequency structures. Also larger area arrays are associated with bigger junction capacitance, which slows down the switching speed. At the same time decreasing the array size too much also has drawbacks. Coupling light into the structure becomes harder due to smaller alignment tolerances and in some cases focussing optics are required to reduce the spot size. Taking these considerations into account, it was decided to use PV arrays with 250 μm diameter. A large multi mode fiber with a core diameter of 200 μm could be butt-coupled to the array, thus eliminating the need for focussing/collimating optics. This arrangement allows for alignment errors up to 50 microns without significantly affecting the PV array performance. Another concern for good layout is that the ratio of optically active area to the total PV array area be large. Regions between device mesas and regions shadowed by contact metal do not contribute to photocurrent even though they are illuminated and hence must be minimized. The circular array with pie shaped detectors, shown in fig. (2.13), minimizes the inactive regions between devices. The big contact pads and airbridges are placed towards the periphery of the array so that the inner region of diameter 200 μm (matched to fiber core) is not blocked by metal. For the structure shown in fig. (2.13), the optically active region occupies 80% of the total area enclosed by the array. Note that the inactive regions can not be made much smaller (limited

by process capabilities), so when the PV array dimensions are reduced, the inactive regions become larger fractions of the total area thus reducing the optical efficiency.

Ohmic Contacts

Next device

Airbridge

P-GaAs   P-GaAs   Next device

N-GaAs   N-GaAs

Substrate Leakage

Semi-insulating GaAs

(a)

Ohmic Contacts

Next device

Airbridge

P-GaAs   P-GaAs   Next device

N-GaAs   N-GaAs

Oxidized AlGaAs   Oxidized AlGaAs

Semi-insulating GaAs

(b)
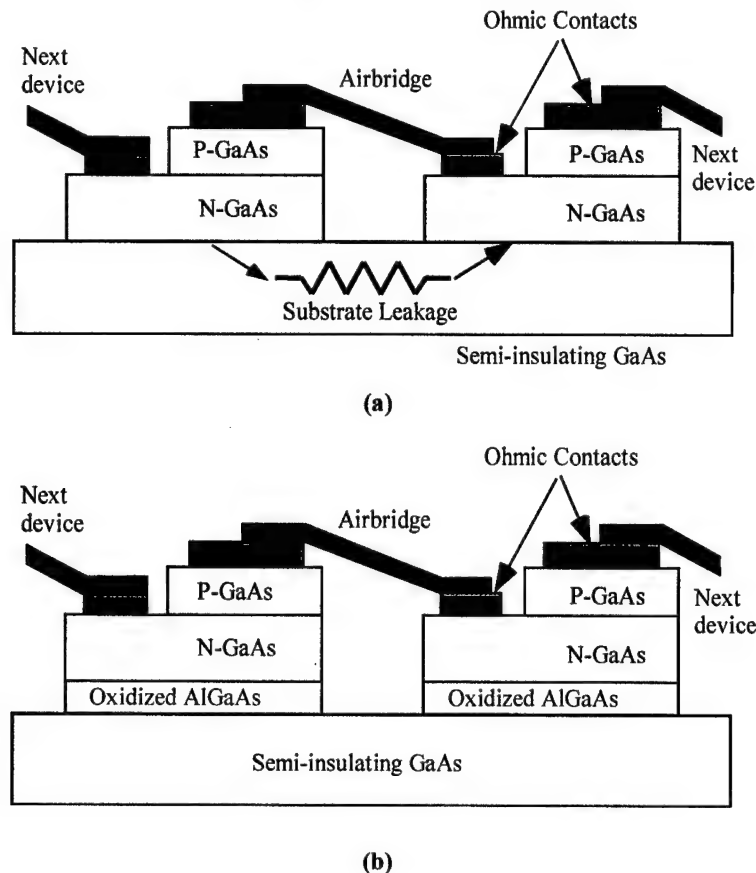
Figure 2.12: a) Leakage path through the substrate due to the presence of photogenerated carriers b) Buried oxide layer to eliminate substrate leakage.
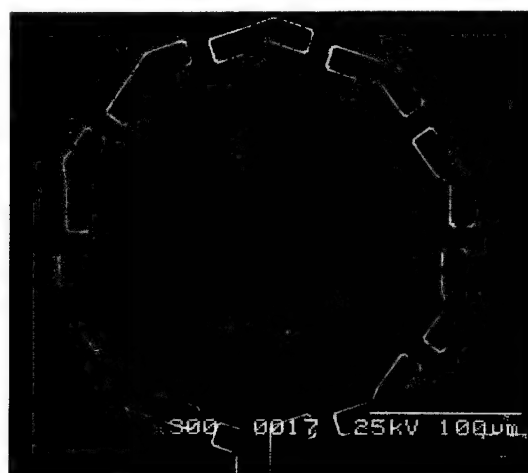
Figure 2.13: Layout of monolithic GaAs PV array, designed and fabricated at UCSB, showing pie shaped detectors connected together by airbridges to form a circular array.

35

2.6 Fabrication of planar GaAs PV cells and arrays

The epitaxial structure of the GaAs wafers used for the fabrication of monolithic PV arrays are shown in fig. (2.14a,b). The structures were grown by Prashant Chavarkar on MBE system B at UCSB. The structure depicted in fig. (2.14a) incorporates a .05 μm thick $Al_{.98}Ga_{.02}As$ layer below the N^+ contact layer. As discussed in the previous section, this $Al_{.98}Ga_{.02}As$ layer is oxidized laterally to form an insulating layer at the base of the device mesa. The structure shown in fig. (2.14b) is the control structure and it does not have the buried $Al_{.98}Ga_{.02}As$ layer for lateral oxidation. The control structure serves as a reference to study the effectiveness of the buried oxide isolation scheme. It also enables us to determine whether the oxidation process has any deleterious effects on the electrical/optical characteristics of the PV cells. Another difference between the two structures is that the control sample does not have the $Al_{.85}Ga_{.15}As$ window layer at the top surface. Thus the effect of the $Al_{.85}Ga_{.15}As$ passivation layer on the surface recombination velocity can be studied. Apart from these differences, the two structures in fig. (2.14a,b) are identical.

$Al_{.85}Ga_{.15}As$ 500Å (passivation)
P^+ GaAs ($N_a = 5\ 10^{18}$) 500Å
P^- GaAs ($N_a = 5\ 10^{17}$) 6000Å
N^- GaAs ($N_d = 2\ 10^{17}$) 7000Å
N^+ GaAs ($N_d = 3\ 10^{18}$) 7000Å
$Al_{.98}Ga_{.02}As$ 500Å (Oxidation)
Semi-insulating GaAs Substrate

(a)

P^+ GaAs ($N_a = 5\ 10^{18}$) 500Å
P^- GaAs ($N_a = 5\ 10^{17}$) 6000Å
N^- GaAs ($N_d = 2\ 10^{17}$) 7000Å
N^+ GaAs ($N_d = 3\ 10^{18}$) 7000Å
Semi-insulating GaAs Substrate
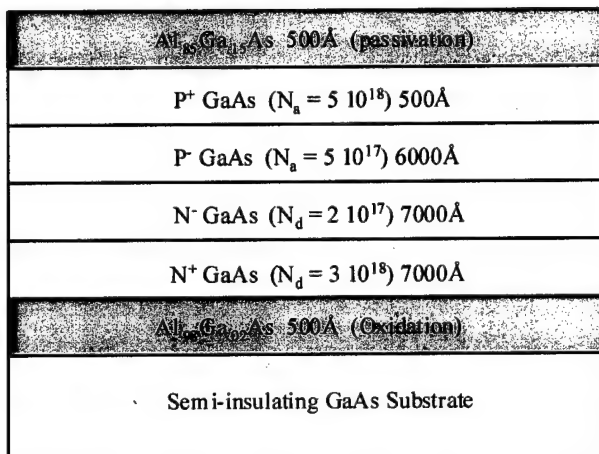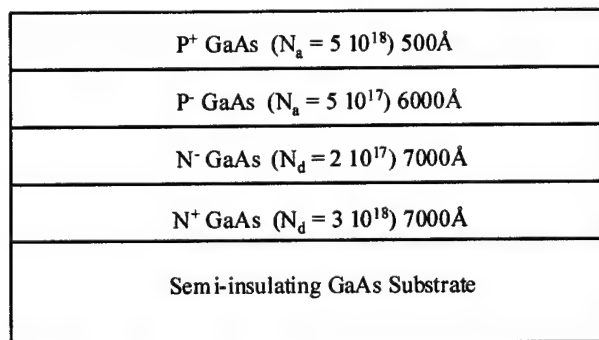
(b)

Figure 2.14: a) Epitaxial layer structure for the oxidized sample b) epitaxial layer structure for the control sample.
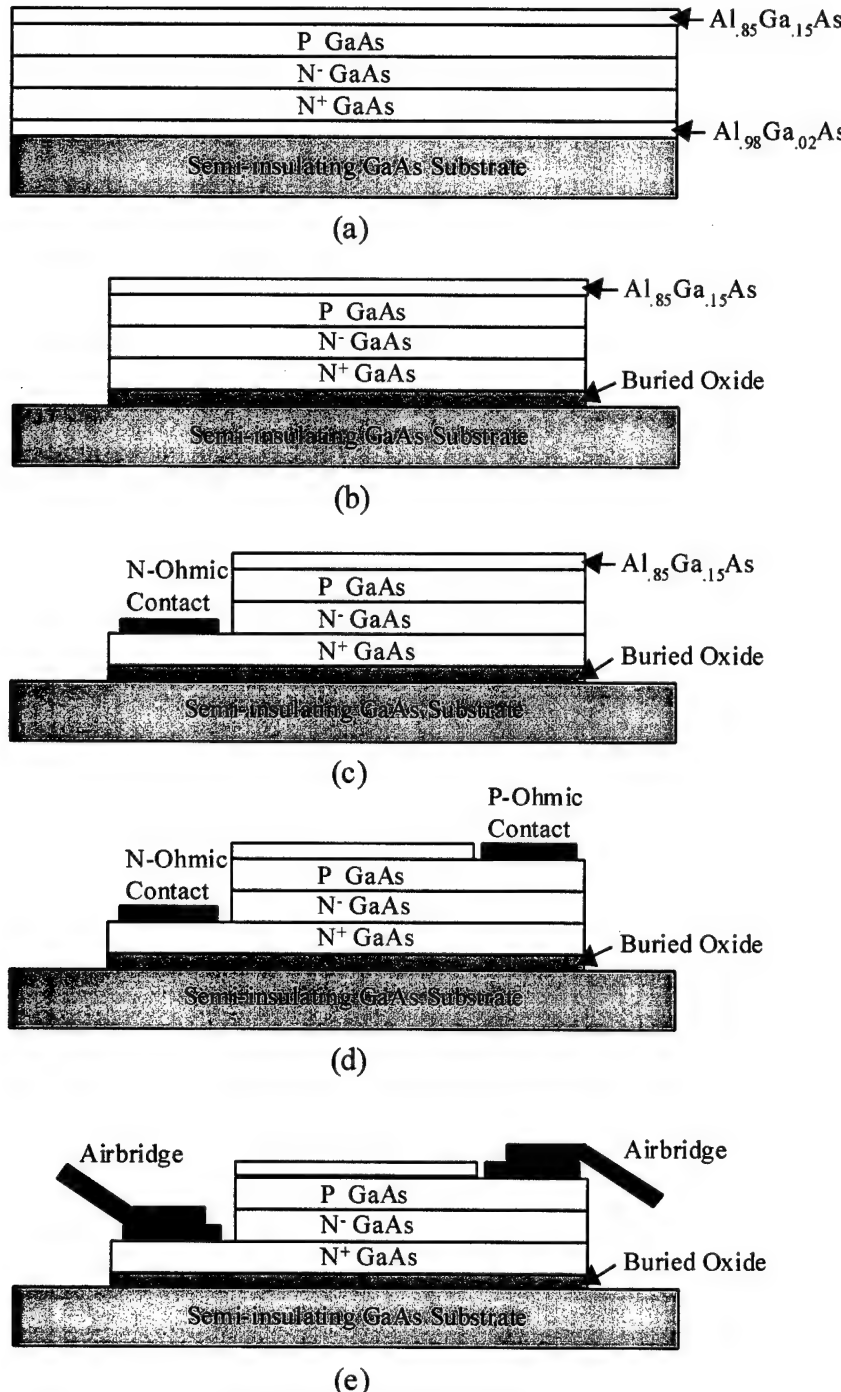
Figure 2.15: Fabrication process for the planar GaAs PV arrays

The fabrication of the monolithic GaAs PV arrays is similar to the fabrication process used for conventional GaAs PN junction diodes except for two changes- the addition of the lateral oxidation step and the stage at which the mesa isolation is carried out. A layer of $Al_{.98}Ga_{.02}As$ is incorporated below the N^+ contact layer during MBE growth of the epitaxial layers and is oxidized in steam using a process

described in [11]. The Oxidation step needs to be carried out before any steps that involve metallization (contacts, airbridges etc.) as it requires exposure to elevated temperatures (430°C) for a long time (40 minutes). Also, since the oxidation proceeds laterally, the diode mesa has to be etched to expose the $Al_{.98}Ga_{.02}As$ layer before it can be oxidized. Hence the mesa etch is the first step in the monolithic PV array process shown in fig. (2.15). At the end of the mesa etch step, thickness variations of the order of 2 μm are present on the wafer surface, which limits line width attainable in the following lithography steps (reason why Schottky contact widths of 2 μm are used). Following the mesa etch, the buried $Al_{.98}Ga_{.02}As$ layer is oxidized in steam at 430°C for 40 minutes. A self-aligned step is used to etch away the P-GaAs and N-GaAs material and Au/Ge/Ni/Au contacts are deposited on the heavily doped N^+ GaAs contact layer. The N-ohmic contacts are alloyed at 420°C for 1 minute. Next the P-ohmic contacts are fabricated by etching away the $Al_{.85}Ga_{.15}As$ window layer and depositing Ti/Au metal on the P^+ GaAs contact layer. Airbridges connecting the cells within each array are fabricated using a two layer resist scheme described in detail in appendix A. Finally a layer of silicon nitride of thickness 0.1 μm is applied to the top surface of the cell as an anti-reflection coating.

Two wafers with the epitaxial structure listed in figure (2.14a,b) were taken through the fabrication process simultaneously. The wafer with the buried oxide layer is referred to as the oxidized sample and the wafer without the buried oxide layer is called the control sample. Note that for the control sample, the oxidation step is eliminated but all other fabrication steps are the same as those for the oxidized sample.

2.7 Characterization of single large area GaAs PV cells

The processed wafers contained single large area PV cells in addition to 10-cell PV arrays that were intended for use in the monolithic OVC. The electrical and optical performance of the single large area PV cells was characterized first and then the properties of the 10-cell PV arrays were measured. The array performance was compared to that of the single PV cells to ensure that the monolithic integration process did not degrade their performance. The electrical properties were characterized (in the absence of illumination) by measuring the I-V curves on a HP4145 Semiconductor Parameter Analyzer. Optical characterization of the devices was performed by recording the I-V curves for different intensities of illumination. The illumination source used here was a semiconductor laser diode operating at a wavelength of 670 nm and capable of producing up to 10 mW of optical power. The light from the laser diode was launched into a large multi mode fiber with core diameter 200 μm. The output end of the fiber was butt coupled to the device under test and was positioned using a fiber probe mounted on a XYZ translator stage.

The I-V curve of a single large area PV cell fabricated on the oxidized wafer is shown in fig. (2.16a,b) on a linear and logarithmic scale. From the linear I-V curve, we can see that the forward turn on voltage for the PN-junction diode is about 1.2 V. For large values of forward bias, the diode current is limited by the series resistance of the diode and this is calculated to be 8.7 Ω. Fig. (2.16b) shows the I-V data on a log scale. The horizontal axis in this plot is the junction voltage and is calculated by subtracting the voltage drop due to the series resistance from the applied bias. Using the slope of the log(I)-V curve in equation (2.5), an ideality factor can be estimated for the devices. As depicted in fig. (2.16b), the ideality factor is 2 for low values of applied forward bias and 1.7 for higher forward bias. This because the actual diode current has an injected component (I_{inj}) and a component due to recombination generation (I_{rg}) as described in equation (2.12).

38

$$I = I_{inj} + I_{rg} = I_0\left(e^{\frac{qV}{kT}} - 1\right) + I_0^{rg}\left(e^{\frac{qV}{2kT}} - 1\right) \qquad (2.12)$$

For low values of forward bias (<0.8 V), the recombination generation component dominates and this explains the n=2 region. For higher forward bias, the injected current starts to dominate, but the total current still has contributions from the recombination term and so the ideality factor is between 1 and 2 (1.7 in this case). The range of voltages around 0.9 V is of interest to us as the photogenerated voltage is of this order. By fitting the measured I-V data in this voltage range to the ideal diode equation, an ideality factor of 1.7 and a reverse saturation current density of 5×10^{-11} A/cm^2 were estimated for the PV cell on the oxidized wafer. Similar values have been reported for PV cells on MBE grown GaAs. The measurements and analyses reported above were repeated for a large area PV cell on the control wafer. The results are shown in fig. (2.17a,b) and are essentially the same as that for the oxidized sample. This tells us that the lateral oxidation step did not adversely affect the electrical properties of the PV cell.

The I-V curves of the single large area cells were also recorded for varying intensities of optical illumination. Fig (2.18a) and fig (2.18b) show the I-V curves under illumination for the oxidized sample and the control sample respectively. As mentioned earlier, these curves were measured at a wavelength of 670 nm. From the I-V curves, the short circuit current and the open circuit voltages were extracted and their dependence on the optical power was studied. Fig (2.19a) depicts the short circuit current of the oxidized and control sample as a function of optical power. As expected, the short circuit current for both samples varies linearly with incident optical power. From the slope of the I_{sc} versus P_{opt} curve the external quantum efficiency was calculated to be 75% for the oxidized sample and 69.6% for the control sample. The higher quantum efficiency for the oxidized sample is believed to be due to reduced surface recombination at the top interface because of the $Al_{.85}Ga_{.15}As$ layer. Note that the quantum efficiency numbers calculated above are external quantum efficiencies and do not take into account the fact that some of the light is reflected at the front surface and that the contacts block some of the light. After accounting for light lost due to these effects, the internal quantum efficiency is calculated to be 85.8% for the oxidized sample and 79.6% for the control sample. Fig. (2.19b) depicts the measured open circuit voltages as a function of the optical power in decibels and shows that the open circuit voltage does indeed vary as the logarithm of the incident optical power. Note that the open circuit voltages are almost identical for both samples. The fill factor and the energy conversion efficiency were also extracted from the I-V data for the large area PV cell on the oxidized wafer and the control wafer. The fill factor was almost equal for both samples but the oxidized sample had a higher energy conversion efficiency of 35.3% compared to the control sample with an energy conversion efficiency of 33.3%. Note that the higher energy conversion efficiency is due to the higher short circuit currents in the oxidized sample, which in turn is attributed to the fact that the $Al_{.85}Ga_{.15}As$ layer reduces surface recombination. The performance of the two samples is summarized in table (2.1). The numbers measure here are comparable with those reported in the literature for planar PV cells [12].

Sample	Quantum efficiency	Fill Factor	Conversion efficiency
Control	69.6%	0.81	33.3%
Oxidized	75%	0.82	35.3%

Table 2.1: Summary of single large area PV cell performance under illumination with 5 mW of optical power at 670 nm.
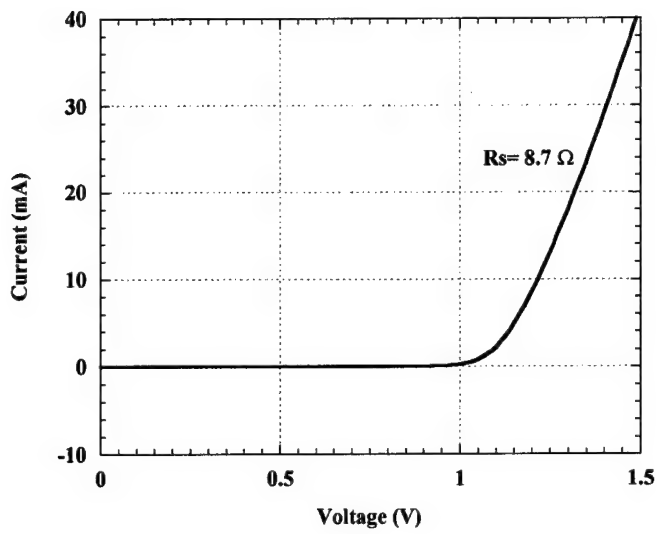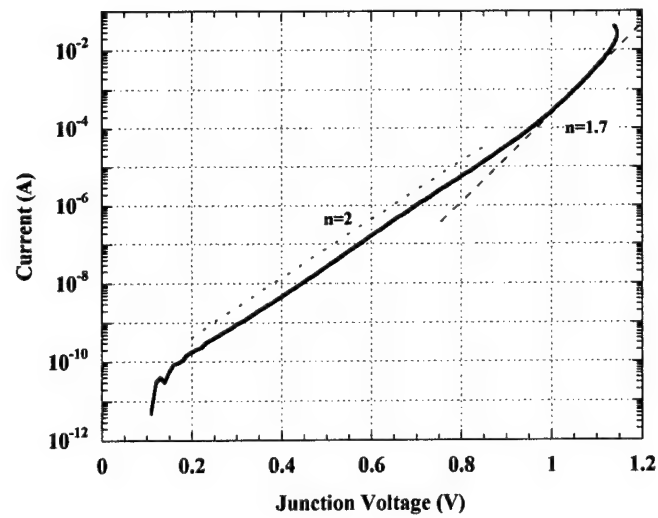
Figure 2.16: Forward I-V curves for a large area PV cell (oxidized sample) in the absence of illumination
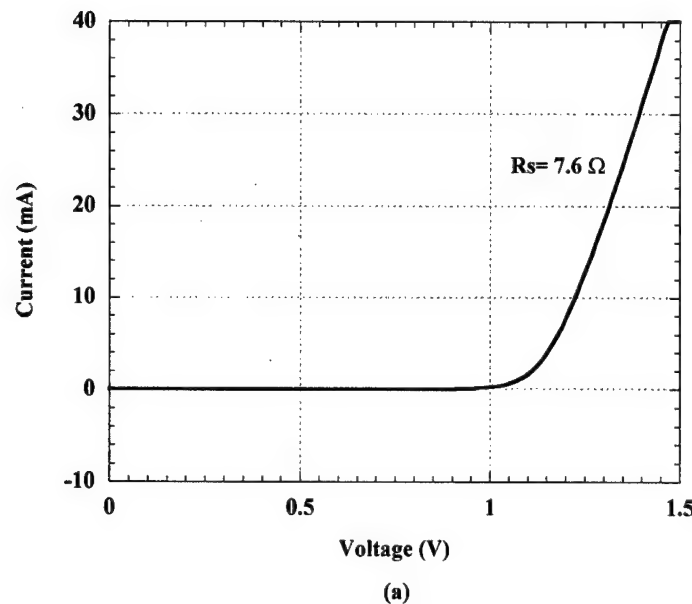
(a)
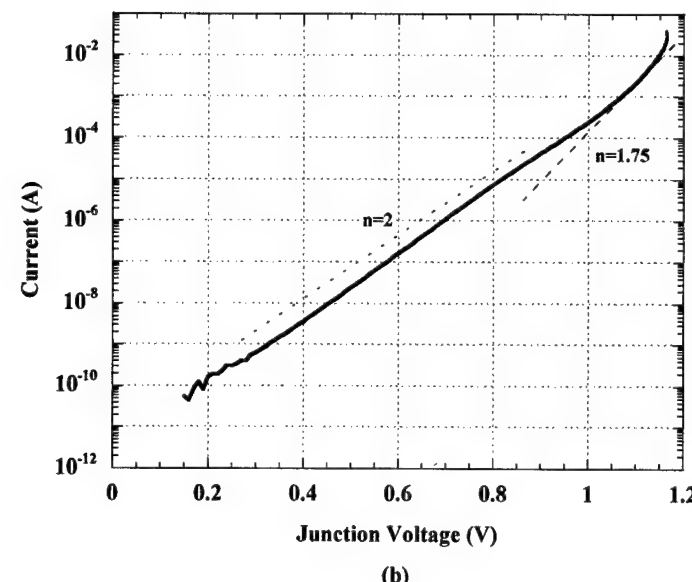

(b)

Figure 2.17: Forward I-V curves for a large area PV cell (control sample) in the absence of illumination
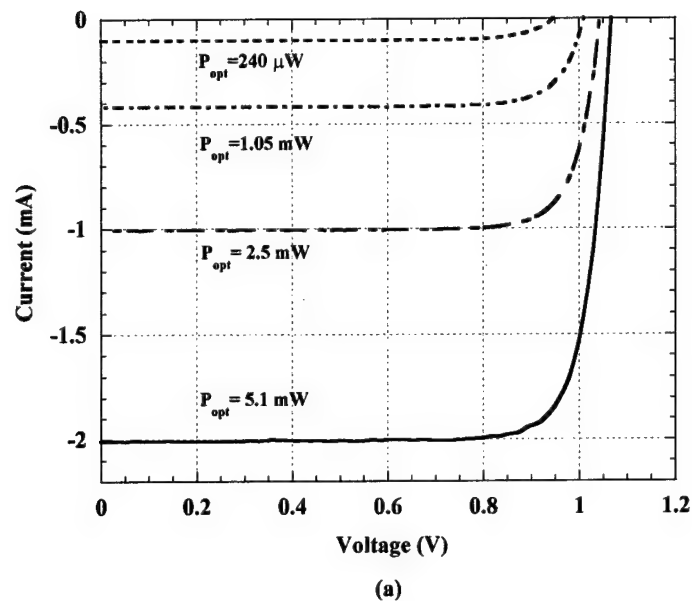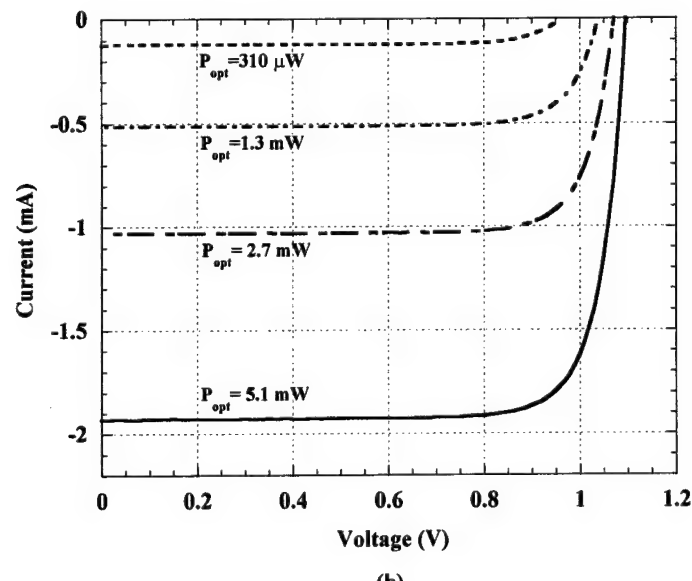
Figure 2.18: I-V curves as a function of illumination for single large area PV cells fabricated on a) oxidized wafer b) control wafer
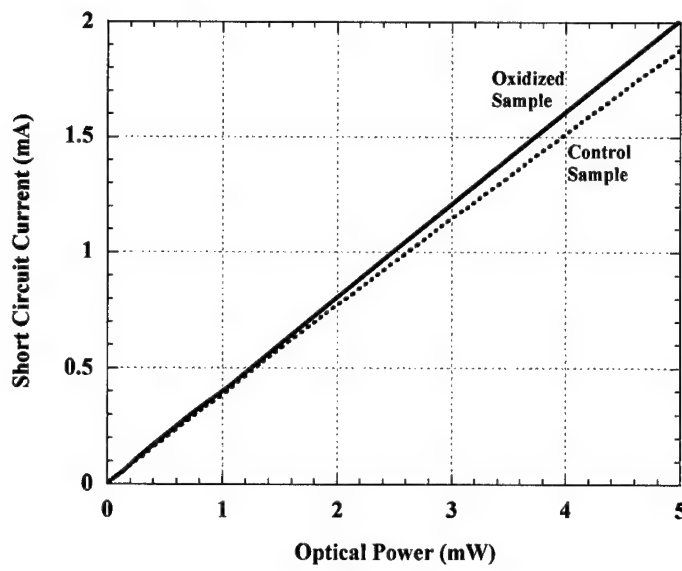
(a)
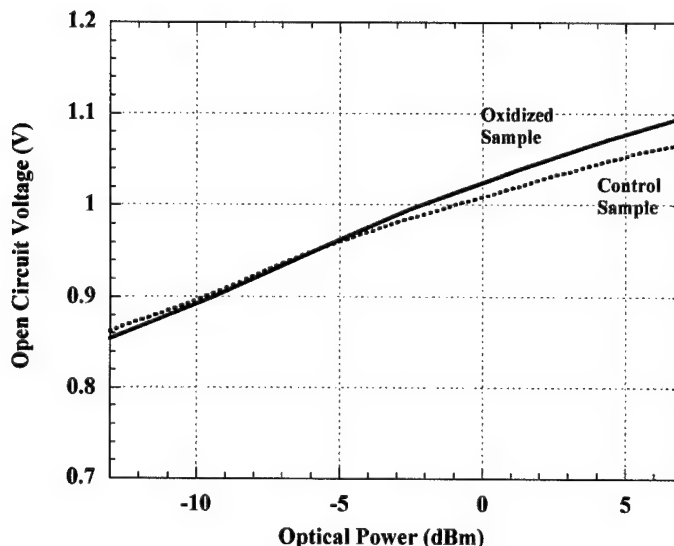
(b)

Figure 2.19: Comparison of the single large area PV cells on the oxidized wafer and the control wafer a) Short circuit current as a function of optical power b) open circuit voltage as a function of optical power.

2.8 Characterization of 10-cell GaAs PV arrays

The dark I-V curve for a 10-cell PV array is shown in fig. (2.20a) on a linear scale. It can be seen that forward conduction through the array turns on at ~12 V which is to be expected since the turn on voltage for a single cell is approximately 1.2 V. The series resistance of the 10 cell array is 64 Ω. The data shown in fig. (2.20a) is for the oxidized sample but the control sample has similar characteristics (in the absence of illumination) as can be verified from the log(I) versus voltage behavior shown in fig. (2.20b). From the slope of the log(I)-V curves, an ideality factor and reverse saturation current for the individual diodes within the array can be computed. This assumes that the applied bias is divided equally among the 10 diodes and is a reasonable assumption since all the diodes are identical. The computed ideality factor for the diodes is 1.9 and the reverse saturation current is 4 10^{-13} A. Note that these values are higher than the corresponding ideality factor and reverse saturation current calculated for single large area PV cells. This can be explained by the fact that the cells within the PV array have a higher perimeter to area ratio than the large area test structures and hence the surface recombination current constitutes a larger fraction of the total diode current for the diodes in the array. The data in fig. (2.20b) confirms that electrically, the PV array behaves like 10 diodes connected in series and that in the absence of illumination, the oxidized sample and the control sample have similar electrical characteristics. The similarity in the dark I-V curves of the oxidized and control sample is to be expected since substrate leakage becomes an issue only when the array is illuminated.

(a)

44
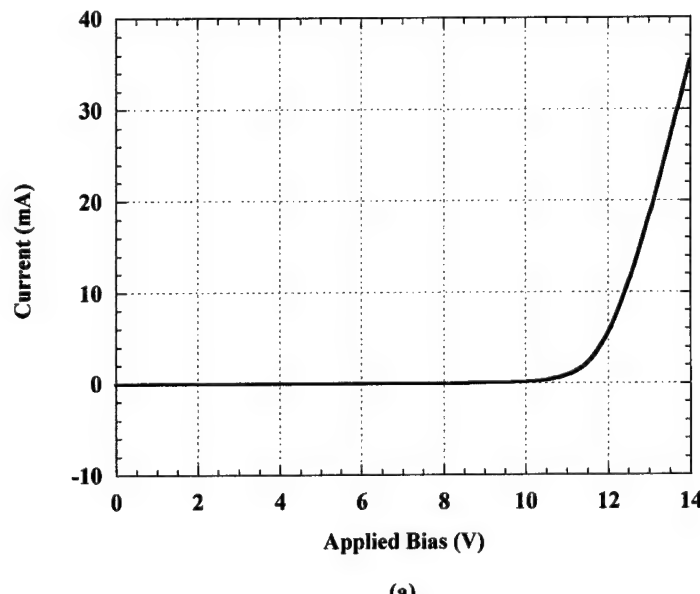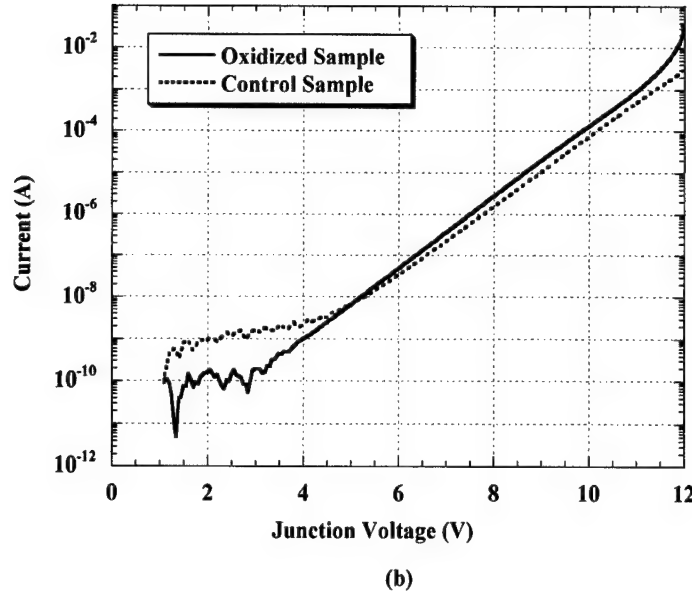
(b)

Figure 2.20: a) I-V curve for a 10-cell PV array on the oxidized wafer b) Comparison of the I-V characteristics of 10-cell PV arrays with and without the buried oxide.

The I-V curves of the 10-cell PV array for various values of illumination intensity are plotted in fig. (2.21a) for the oxidized sample and in fig. (2.21b) for the control sample. The extracted short circuit current and open circuit voltage as a function of optical power are depicted in fig (2.22a,b). Since the voltage across the array is zero under short circuit conditions, the substrate leakage current is zero and hence both the samples have similar short circuit currents. However, under open circuit conditions, the photogenerated voltage causes some of the photocurrent to flow through the substrate leakage path for the control sample. The oxidized sample is effectively isolated from the substrate and hence the entire photocurrent flows through the series of PN junctions. This explains the higher open circuit voltages seen in the case of the oxidized sample. The effect of substrate leakage can be seen clearly in fig. (2.23a) where the I-V curves for the oxidized sample and the control sample are shown side by side. Besides reducing the open circuit voltages, substrate leakage also adversely affects the fill factor and energy conversion efficiency. Table (2.2) compares the performance of 10-cell PV arrays with and without the buried oxide. The fill factor of the oxidized sample is 0.84 and that for the control sample is 0.44. The energy conversion efficiency for the oxidized sample is 26.8% while that for the control sample is only 13.3%. From this data it can be seen that the buried oxide layer is effective in preventing substrate leakage.

Note that even for the oxidized array, the energy conversion efficiency is lower than that of a single large area PV cell (35.3%). The reason for this disparity is that some of the incident optical power is absorbed in the inactive regions between the device mesas. As indicated earlier, the ratio of the optically active area to the total array area is 0.8, which explains why the efficiency is correspondingly lower.

45

Sample	Open circuit voltage	Fill Factor	Conversion efficiency
Control	9.95 V	0.44	13.3%
Oxidized	10.5 V	0.84	26.8%

Table 2.2: Summary of 10-cell PV array performance under illumination with 5 mW of optical power at 670 nm.
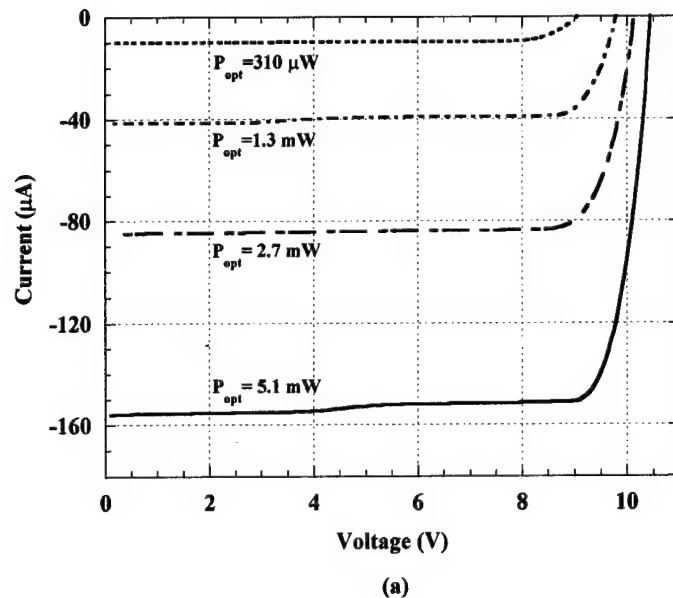

(a)
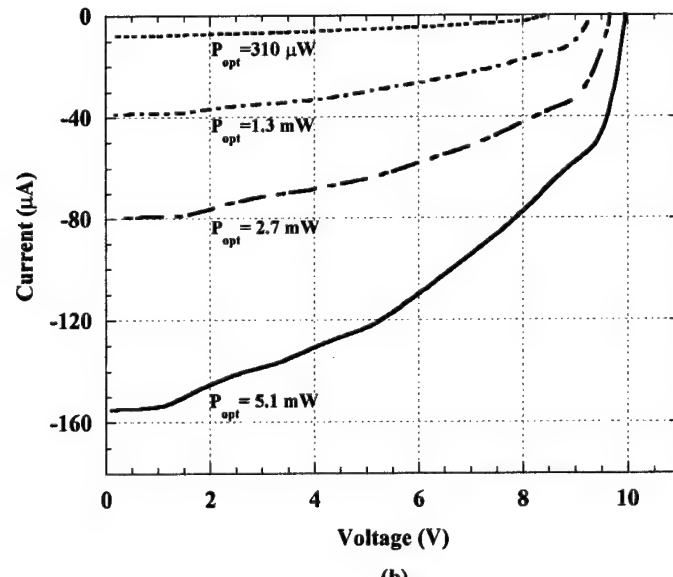
(b)

Figure 2.21: I-V curves as a function of illumination for 10-cell PV arrays fabricated on a) oxidized wafer b) control wafer

46
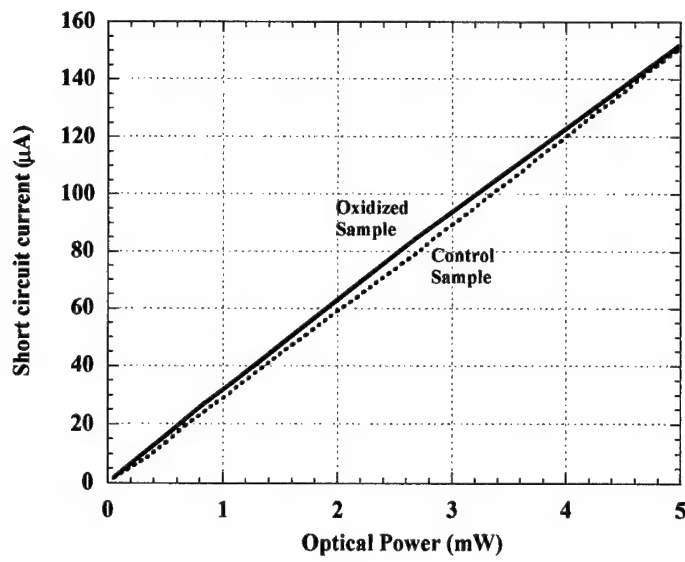
(a)
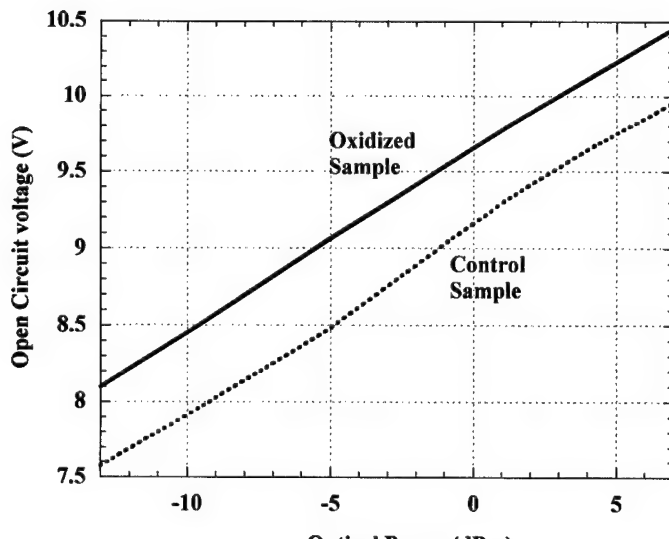
(b)

Figure 2.22: Comparison of the 10-cell PV arrays on the oxidized wafer and the control wafer a) Short circuit current as a function of optical power b) open circuit voltage as a function of optical power.

2.9 Effect of DC loads on the performance of 10-cell PV arrays

As discussed in the previous section, a fixed DC load resistance is connected across the PV array in the OVC. This resistance acts as a discharge path for the array and improves the switching speed. The other advantage of using this resistor is that it helps to "linearize" the output voltage versus optical power response. From fig. (2.22b) it can be observed that the output voltage increases as the log of the optical power under the open circuit conditions. This makes the voltage very sensitive at low illuminations and less sensitive for higher illuminations. In fact, in going from no illumination to a very small optical power (50 μW), the array output voltage increases from 0 V to 8.1 V in the open circuit case. This situation is undesirable since it requires extremely accurate control of the optical power. As shown in fig. (2.23b), the fixed DC load resistance addresses this problem. The output voltage increases linearly for low optical power and eventually becomes a logarithmic function at high optical power. Note however that the reduced sensitivity comes at the cost of increased optical power requirements. The smaller the value of load resistance, higher is the optical power required to generate a given output voltage

The ability of a PV array to drive a load is linked to its fill factor. Since the control sample has a much lower fill factor than the oxidized sample it can not effectively drive small loads. This is indicated in fig. (2.23b) where it can be seen that for a given optical power and load resistance, the control sample generates a lower voltage than the oxidized sample. Also, the disparity in the output voltages between the control sample and the oxidized sample becomes larger as the value of the load resistance is decreased. To realize the importance of this effect, let us consider an application that requires the PV array to generate up to 8 V across a 500 KΩ load. In the case of the oxidized sample, 500 μW of optical power would be required where as the control sample would need an optical power 0f 1.3 mW to drive the same load to 8 V. This emphasizes the importance of the buried oxide layer in reducing the optical power consumption.

(a)

48
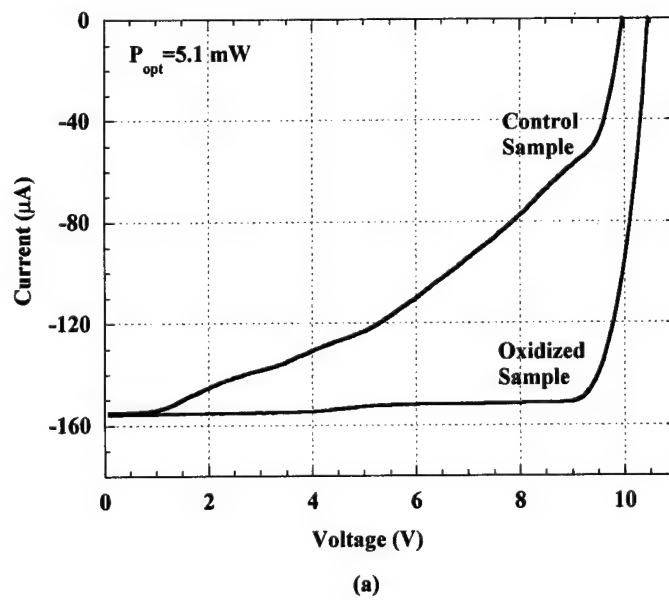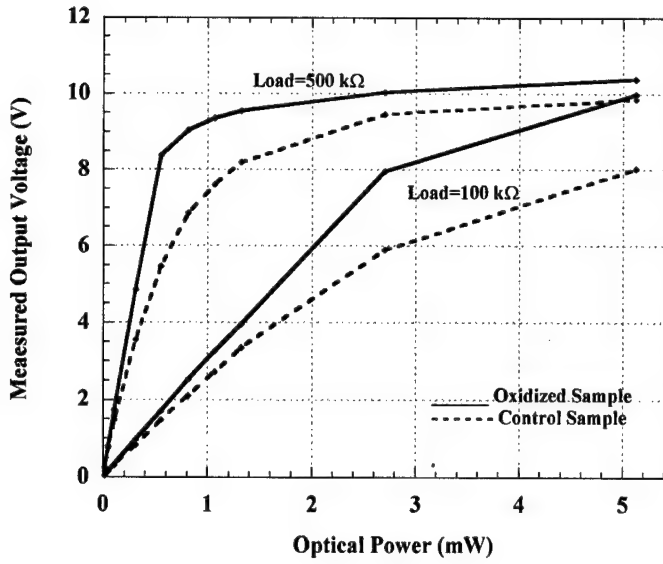
(b)

Figure 2.23: a) Comparison of I-V curves of 10-cell PV arrays fabricated on the oxidized wafer and the control wafer. b) Array output voltage for various DC load values.

An equivalent circuit model for the illuminated 10-cell PV array under DC loading is shown in fig. (2.24a). The model consists of 10 PN diodes in series, connected in parallel with a current source that accounts for the photogenerated current. Note that this model implicitly assumes that all the diodes are being illuminated uniformly and that the photocurrent generated in each is identical. This assumption is reasonably good for the circular array configuration and provides a good starting point for analysis. The diodes are assumed to have an ideality factor of 1.9 and reverse saturation current of $4 \ 10^{-13}$ A based on the measured I-V data. The amplitude of the photocurrent is calculated from the optical power since the quantum efficiency of the diodes is known. Using the parameters discussed above for the elements of the equivalent circuit model, the output voltage of the PV array driving a DC load was simulated on the HP EEsof DC Test Bench. The simulation results showed good agreement with the measured data as depicted in fig. (2.24b). Hence the equivalent circuit model of fig. (2.24a) can accurately predict the PV array output voltage as a function of optical power as well as DC load resistance.

Thus, planar GaAs PV arrays have been successfully fabricated alongside planar GaAs Schottky varactor diodes (on the same wafer) using monolithic fabrication and integration techniques. A novel buried oxide isolation scheme was utilized in the monolithic PV arrays to prevent substrate leakage under illumination. The PV arrays with the buried oxide isolation are capable of generating up to 10.5 volts under illumination and have fill factors and energy conversion efficiencies as high as 0.84 and 26.8 % respectively. The high fill factor and conversion efficiency enables the PV array to drive DC loads with small optical powers. This plays an important role in reducing the optical power requirements of the OVC, as will be discussed in more detail in the following section.

49
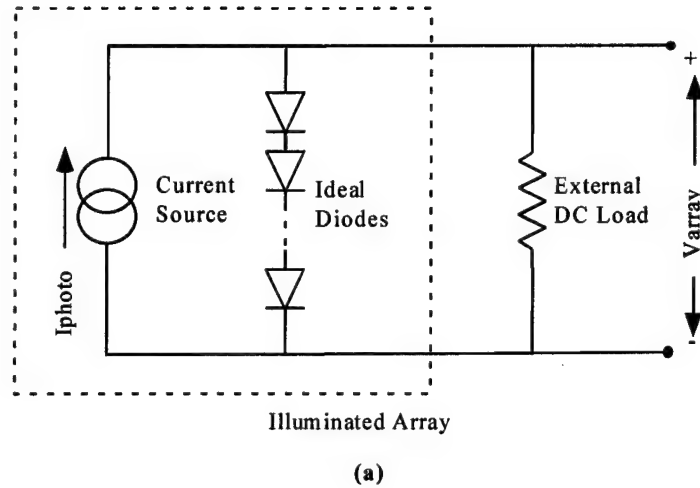
(a)
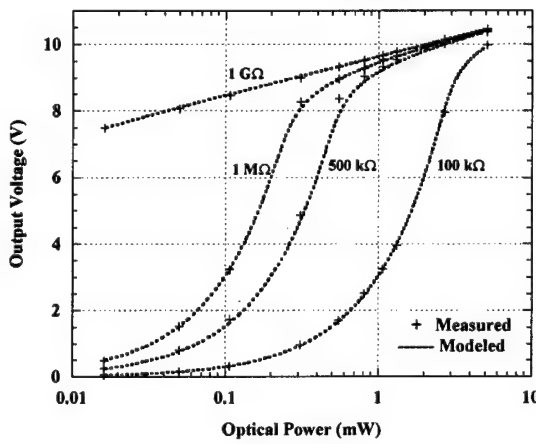
(b)

Figure 2.24: a) Equivalent circuit model for 10-cell PV array driving an external DC load b) Comparison of simulated and measured array output voltage.

References

[1]   M. J. W. Rodwell, M. Kamegawa, R. Yu, M. Case, E. Carman, and K. S. Giboney, "GaAs nonlinear transmission lines for picosecond pulse generation and millimeter-wave sampling," *IEEE Transactions on Microwave Theory and Techniques*, vol. 39, pp. 1194-2041991.

[2]   S. T. Allen, "Schottky Diode Integrated Circuits for Sub-Millimeter-Wave Applications," *Ph.D. Thesis*: University of California at Santa Barbara, 1994.

[3]   S. T. Allen, U. Bhattacharya, and M. J. W. Rodwell, "Multi-terahertz sidewall-etched varactor diodes and their application in submillimetre-wave sampling circuits," *Electronics Letters*, vol. 29, pp. 2227-8, Dec. 1993.

[4]   H. J. Hovel, *Solar cells*, Semiconductors and semimetals;vol. 11: Acadenic Press, New York, 1975.

[5]   M. R. Melloch, S. P. Tobin, T. B. Stellwag, C. Bajgar, A. Keshavarzi, M. S. Lundstrom, and K. Emery, "High-efficiency GaAs solar cells grown by molecular-beam epitaxy," in *J. Vac. Sci. Technol. B, Microelectron. Process. Phenom. USA*, Raleigh, NC, USA, 1989, vol. 8, pp. 379-83.

[6]   J. M. Woodall and H. J. Hovel, "High-efficiency Ga/sub 1-x/Al/sub x/As-GaAs solar cells," *Applied Physics Letters*, vol. 21, pp. 379-81, Oct. 1972.

[7]   G. C. DeSalvo and A. M. Barnett, "Investigation of alternative window materials for GaAs solar cells," *IEEE Transactions on Electron Devices*, vol. 40, pp. 705-11, April. 1993.

[8]   A. Saletes, J. P. Contour, M. Leroux, J. Massies, N. Defranould, and G. Pelous, "GaAlAs/GaAs solar cells grown by molecular beam epitaxy: material properties and device parameters," *Solar Cells*, vol. 17, pp. 373-81, M. April. 1986.

[9]   A. S. Nagra, P. Chavarkar, C. J. Swann, T. Larry, M. L. VanBlaricum, U. K. Mishra, and R. A. York, "Monolithic optically variable capacitors for tunable microwave antennas," in *Proceedings. IEEE/Cornell Conference on Advanced Concepts in High Speed Semiconductor Devices and Circuits*, Ithaca, NY, USA, 1997, , pp. 69-78.

[10]   A. S. Nagra, M. L. VanBlaricum, and R. A. York, "Low -power indirect optical reactance control using monolithic GaAs OVC technology," in *Photonic systems for Antenna Applications Symposium Proceedings*, Monterey, CA, 1998, , pp.

[11]   P. A. Parikh, P. M. Chavarkar, and U. K. Mishra, "GaAs MESFET's on a truly insulating buffer layer: demonstration of the GaAs on insulator technology," *IEEE Electron Device Letters*, vol. 18, pp. 111-131997.

[12]   W. W. Ng, K. Nakano, Y. Z. Liu, and P. D. Dapkus, "A monolithic GaInAsP/InP photovoltaic power converter," *IEEE Transactions on Electron Devices*, vol. ED-29, pp. 1449-54, Sept. 1982.

Demonstration of the Monolithic OVC in Microwave Circuits and Antennas

This section deals with the fabrication and testing of the monolithic OVC and its demonstration in microwave circuits and antennas. Using monolithic techniques, GaAs PV arrays, Schottky varactor diodes and resistors were simultaneously fabricated on the same wafer and integrated to form the complete OVC. The monolithic OVC was subsequently incorporated into monolithic microwave circuits and antennas. Details of the fabrication and integration techniques are reported here. Microwave performance of the individual OVC and the circuits/antennas that incorporate the OVC is also presented. Optical control of band reject filters, x-band analog phase shifters and folded slot antennas has been demonstrated. The circuits/antennas mentioned above did not require external DC bias and less than 500 µW of optical power was needed for the maximum tuning/control range. This is the lowest reported optical power requirement for bias free optical control of microwave circuits. Also, the transient response of the OVC was measured and it was demonstrated that the rise/fall times of the OVC could be made less than 1 µs (which is fast enough for several microwave control applications). Thus, this section demonstrates the feasibility of the monolithic OVC technology for low power, bias-free control of microwave circuits and antennas.

3.1 Monolithic integration of the OVC components

The monolithic OVC consisted of a GaAs PV array, a varactor diode and a RF-blocking resistor connected as shown in fig. (3.1a). The GaAs PV array consisted of 10 planar PN-junction photovoltaic cells, connected in series to form a circular PV array. The varactor diode employed in the OVC was a planar Schottky diode. The design, fabrication and testing of the 10-cell GaAs PV array and the Schottky varactor diode have been described in detail in section 2. The RF-blocking resistor was of 2.5 KΩ value and was fabricated on-wafer using NiCr as the resistive layer. The NiCr layer (50nm thick) had a sheet resistance of 40 Ω/square and so the resistor was designed to have a length to width aspect ratio of 62.5. CPW contact pads were provided to enable microwave measurements on the OVC and also to make it easy to incorporate the monolithic OVC into microwave circuits/antennas. The connections between the individual components within the OVC, as well as to the CPW pads, were made using monolithically fabricated airbridges. A schematic of the layout of the monolithic OVC is shown in fig. (3.1b).

Note that in fig. (3.1a) the DC load resistor is shown external to the monolithic OVC. The DC load resistor is the only component of the OVC that was not fabricated and integrated using monolithic processing techniques. As discussed in section 2, this DC load resistance is required to reduce the sensitivity of the PV array for low illumination intensities and to increase the switching speed. Since this resistance must large (100 KΩ-1 MΩ), it was not implemented on wafer. A miniature chip resistor of value 100 KΩ-1 MΩ was wire bonded to the OVC circuit to provide the DC load. Connection parasitics due to the wire bonds were not a concern since this load resistor only affects the DC performance and acts like an open circuit at microwave frequencies.
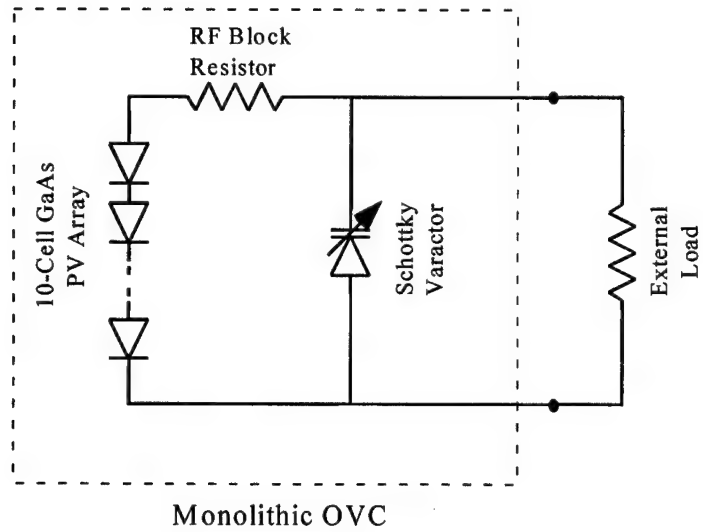
(a)
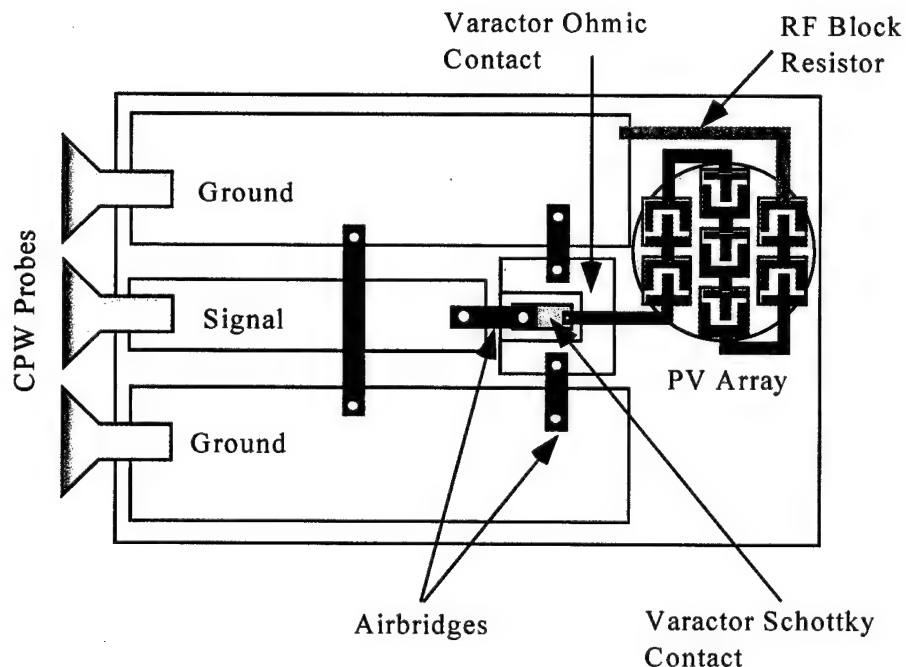
(b)

Figure 3.1: (a) Components of the monolithic OVC (b) Layout of the monolithic OVC.

PV cell mesa

P- GaAs
N- GaAs
N+ GaAs

Schottky diode mesa

P- GaAs
N- GaAs
N+ GaAs

—Oxidized AlGaAs—
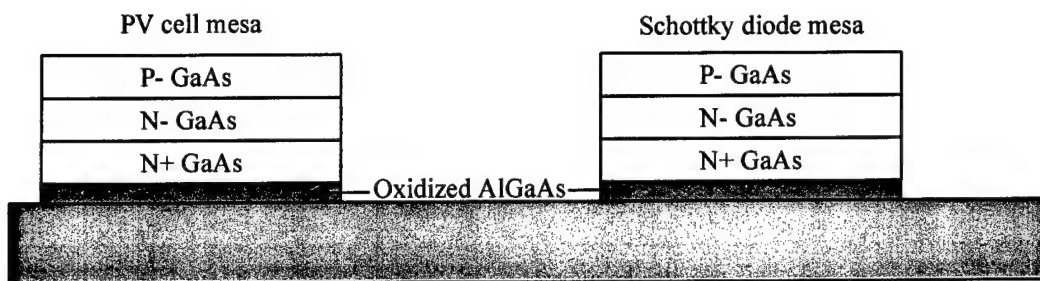
(a) Mesa etch and lateral oxidation

PV cell mesa

P- GaAs
N- GaAs
N+ GaAs

Schottky diode mesa

N- GaAs
N+ GaAs

—Oxidized AlGaAs—
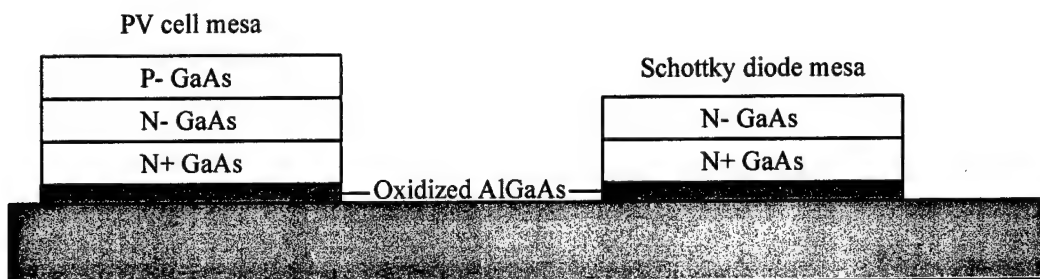
(b) Expose top of Schottky mesa

P- GaAs
N- GaAs
N+ GaAs

N-ohmic

N- GaAs
N+ GaAs

N-ohmic

—Oxidized AlGaAs—

(c) Self aligned N-ohmic contacts

P- GaAs
N- GaAs
N+ GaAs

N-ohmic

Schottky contact

N- GaAs
N+ GaAs

N-ohmic

—Oxidized AlGaAs—

(d) Schottky contact

54
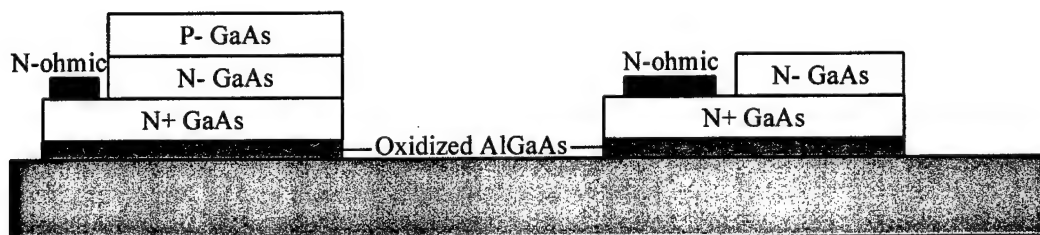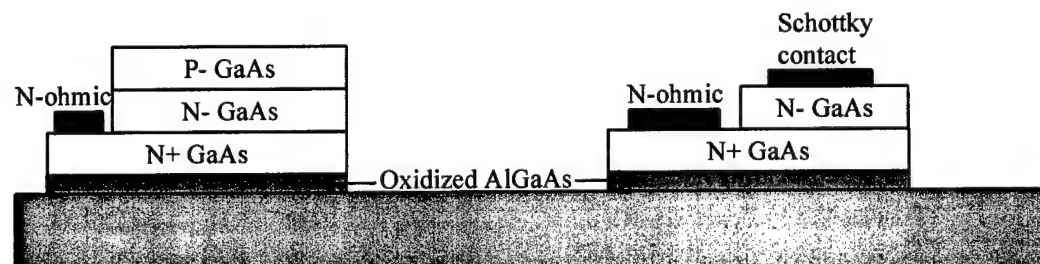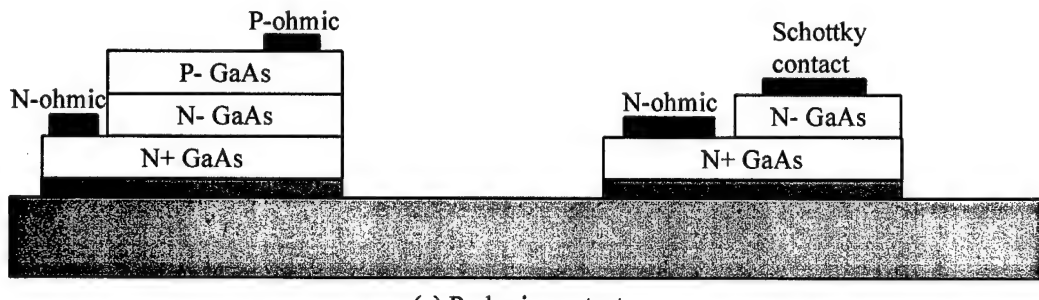
(e) P-ohmic contacts
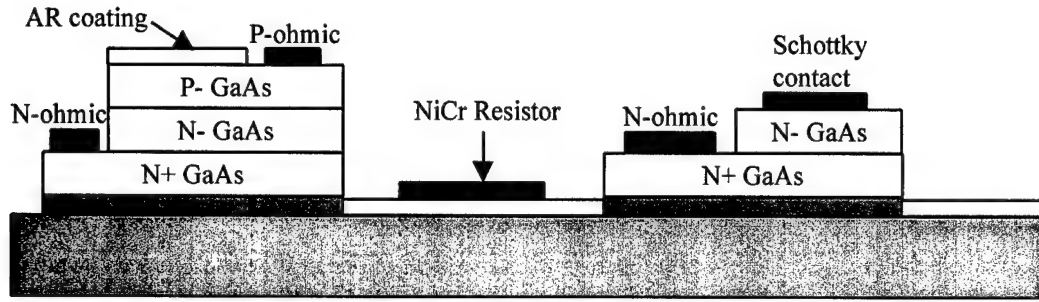
(f) AR coating and NiCr resistors
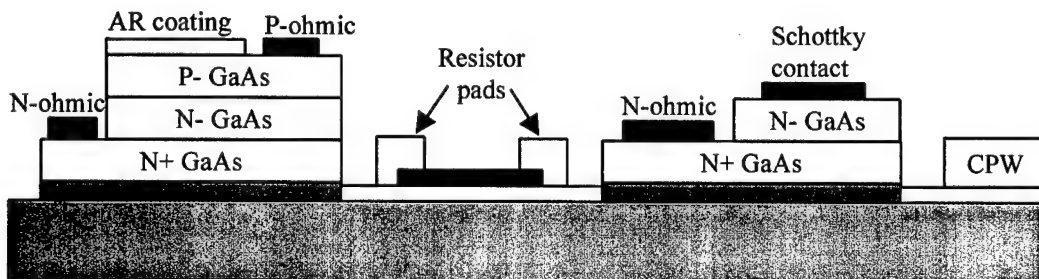
(g) CPW metal and resistor pads
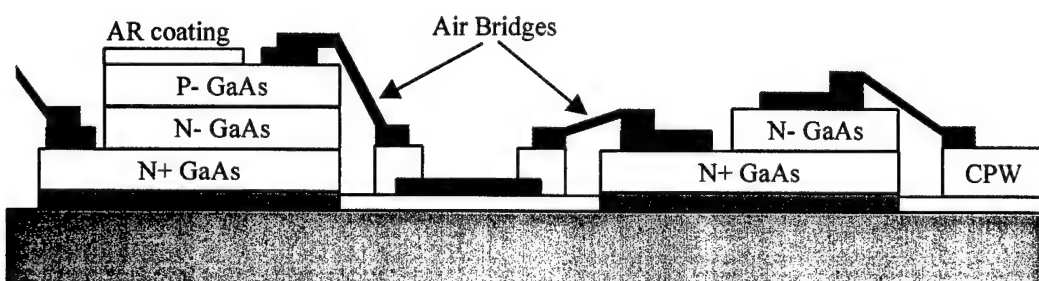

(h) Air bridge interconnections

Figure 3.2: Fabrication process flow for the monolithic OVC

A brief description of the fabrication process for the monolithic OVC is given here and detailed processing instructions are included in appendix A. The process flow schematic in fig. (3.2) depicts the simultaneous fabrication of the individual OVC components and their eventual integration. The first step is the definition of the active mesa regions for the PV cells and the Schottky diodes. The material surrounding the active mesas is removed by RIE etching away the GaAs layers down to the semi-insulating substrate. The next step is the lateral oxidation of the $Al_{.98}Ga_{.02}As$ layer at the bottom of the device mesas. The lateral oxidation of the $Al_{.98}Ga_{.02}As$ is carried out in the presence of steam in a furnace at 430° C. At the end of this step the all the mesa regions have been effectively isolated. The next step is the removal of the P-type GaAs material on the Schottky mesas to expose the lightly doped N⁻ GaAs layer, which is the topmost layer for the Schottky diodes. Self-aligned N-ohmic contacts are made by etching down to the heavily doped N⁺ GaAs contact layer and depositing AuGe/Ni/Au. The contacts are alloyed at 430° C for 1 minute. Note that the N-ohmic contacts for the PV cells and the Schottky varactor diode are fabricated in the same step. The varactor diodes are completed when Pt/Au is deposited as the Schottky contact layer on the lightly doped N- GaAs layer on the Schottky mesa. Note that this step does not affect the PV cell mesa. The PV cells are completed by depositing a non-alloyed Ti/Au contact on the heavily doped P+ GaAs layer on the PV cell mesas. Next a layer of silicon nitride (Si_3N_4) of thickness 85 nm is deposited over the entire wafer. This layer serves as the anti-reflection coating for the optically active PV cell mesas. The Si_3N_4 layer lying on the semi-insulating substrate acts as the insulating barrier on which the NiCr resistor and CPW metal can be deposited. This insulating layer prevents optically generated carriers in the substrate from leaking into the resistor/CPW metal. The RF-blocking resistor is fabricated by depositing a layer of NiCr of thickness 50 nm on top of the silicon nitride layer. The next step is the evaporation of 1.5 μm thick Ti/Au to form the CPW pads and the resistor contacts. Finally all the components are connected using a two-step air bridge process described in detail in appendix A.

A picture of the monolithic OVC fabricated at UCSB is shown in fig. (3.3a). The circular PV array, RF-blocking resistor, Schottky varactor diode, CPW pads and airbridges used for connections are clearly visible.

3.2 Microwave characterization of the monolithic OVC

The microwave performance of the monolithic OVC was tested on a Cascade RF probe station with X-Y-Z translator stages on which ACP-40 CPW probes were mounted. The CPW probes were connected to a HP 8510 network analyzer to make s-parameter measurements. The measurement setup was calibrated using the Line Reflect Match (LRM) calibration scheme developed by Cascade Microelectronics. The illumination for the OVC was provided by a semiconductor laser diode operating at a wavelength of 670 nm. The output from the laser was coupled into a multi-mode fiber with a core diameter of 200 μm. The output end of the fiber was aligned vertically over the OVC using a fiber probe mounted on a X-Y-Z translator stage. Fig. (3.3b) shows a picture of the measurement setup and the CPW probes and the fiber probe can be clearly seen over the stage bearing the OVC wafer.
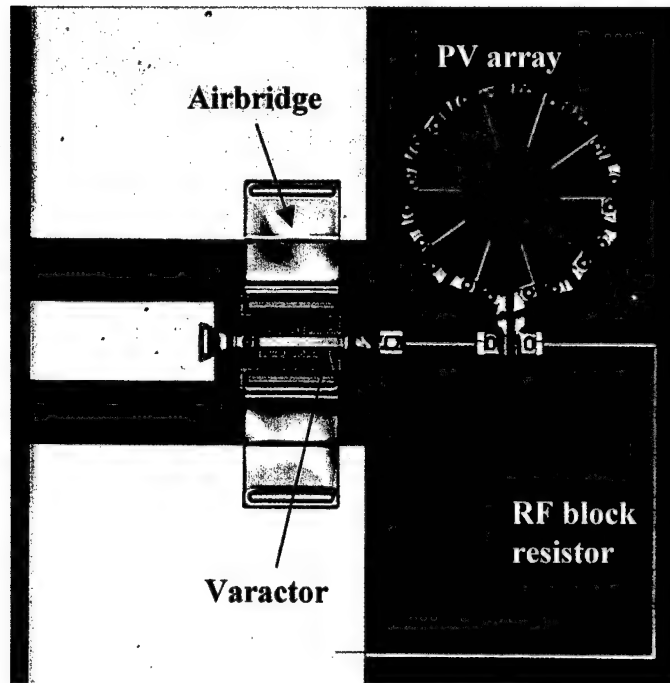
(a)
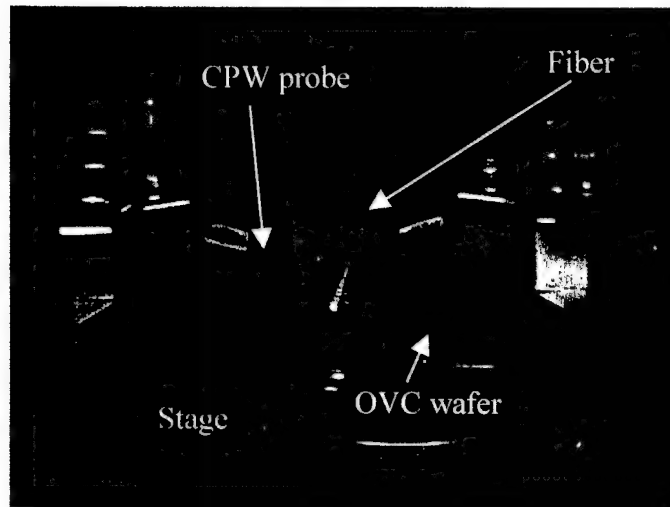
(b)

Figure 3.3: (a) Picture of monolithic OVC fabricated at UCSB (b) photograph of the measurement setup used for microwave characterization of the monolithic OVC.

The s-parameters of the OVC were recorded as a function of optical illumination over the frequency range of interest. At microwave frequencies, the RF-blocking resistor effectively acts like an open circuit and so the PV array makes negligible contribution to the RF performance of the OVC. Thus the OVC essentially

57

behaves like a varactor diode at the end of CPW pads. Hence the same technique that was used for characterization of the Schottky varactor diode was used here to study the microwave characteristics of the OVC. In order to de-embed the OVC from the CPW pads, an on-wafer reference standard comprising of probe pads terminated with a short circuit was used to set the reference plane at the position of the OVC. The measured one port s-parameter (S11) was converted to an equivalent admittance (Y) and fitted to a simple series RC model using the method described in [1, 2]. The OVC capacitance extracted from the s-parameter data is shown as a function of optical power in fig. (3.4). It can be seen that the OVC capacitance varies from 0.85 pF to 0.38 pF when the optical power is increased from 0 μw to 200 μW. Thus a capacitance swing by a factor of 2.2 was achieved with just 200 μW of optical power. Note that the DC load resistor for this measurement was 1 MΩ and was due to the impedance of the probing setup.

The variation of the OVC capacitance with optical power was modeled using the measured characteristics of the individual OVC components. As discussed in the previous section, the PV array output voltage has been recorded for different optical powers and DC load resistances. The variation of the Schottky varactor capacitance with applied bias has also been studied. By combining this data, a curve for the expected OVC capacitance variation with optical power was generated. As shown in fig. (3.4), the modeled capacitance versus optical power curve and the capacitance extracted from the s-parameter data show reasonably good agreement. The extracted capacitance is about 0.04 pF higher than the expected capacitance and this can be attributed to fringing capacitance not accounted for in the model.

Monolithic microwave circuits such as band reject filters and x-band analog phase shifters, which incorporated the OVC as the optically controlled reactive element, were designed and fabricated. Folded slot antennas with shunt OVCs for impedance tuning were also fabricated and tested. Bias free optical control of these circuits/antennas was demonstrated and the details are provided in the following sections.
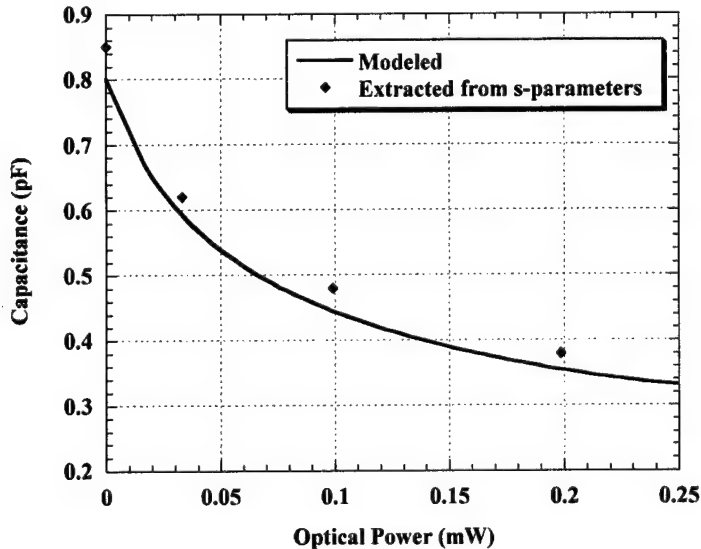

Figure 3.4: OVC capacitance variation with optical power.

3.3 Optically tunable band-reject filter

One of the simplest circuits designed to demonstrate optical control using the monolithic OVC was the optically tunable band reject filter. The circuit was fabricated on GaAs using monolithic techniques and shared the same process steps as the OVC. A picture of an optically tunable band reject filter circuit fabricated at UCSB is shown in fig. (3.5a). The CPW lines for the input and output of the microwave signal, the CPW resonator, and the OVC are clearly visible.


(a)

(b)
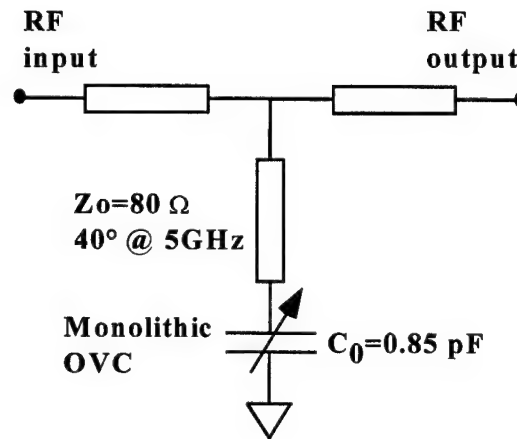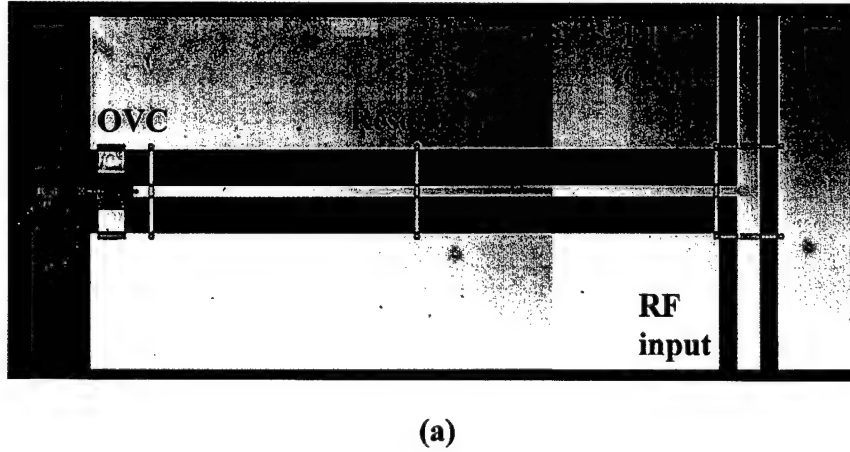
Figure 3.5: (a) Picture of optically tunable band reject filter fabricated at UCSB (b) equivalent circuit for the optically tunable band reject filter.

The equivalent circuit for the optically tunable band reject filter is given in fig. (3.5b) and shows an OVC (zero bias capacitance 0.85 pF) placed at the end of a shunt stub of impedance 80 Ω and length 2.5 mm. The basic principle of operation of this circuit is fairly straightforward. The stub loaded with the OVC acts as the resonator whose electrical length determines the resonance frequency. At resonance, the OVC-loaded shunt stub appears like a short circuit, causing the microwave signal to be reflected. Hence

59

frequencies in the vicinity of the resonance frequency are not transmitted through the structure resulting in band reject characteristics. Due to the optically variable capacitance loading the shunt stub, the resonance frequency and hence the rejection band can be tuned optically.
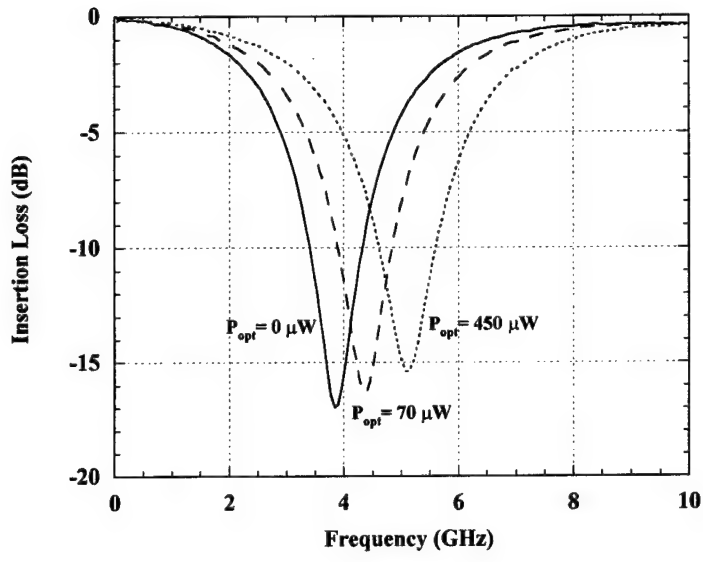
(a)
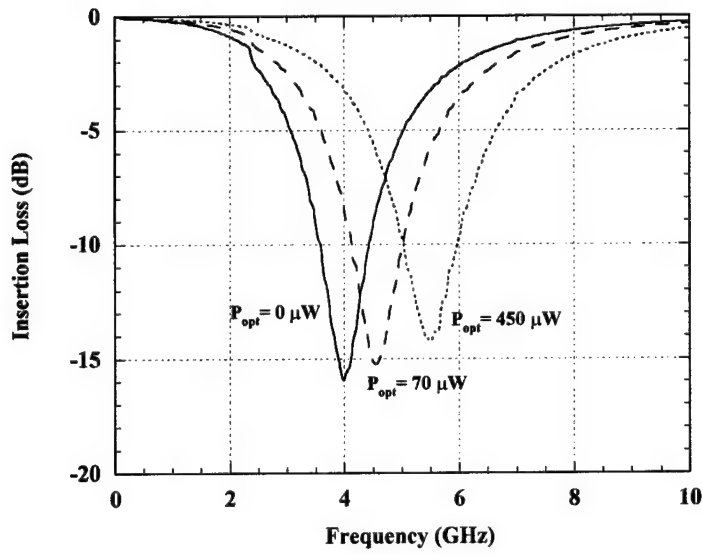
(b)

Figure 3.6: (a) Measured response of the optically tunable band reject filter (b) simulated response of the optically tunable band reject filter.

The measured performance of the optically tunable band reject filter fabricated at UCSB is shown in fig. (3.6a). Note that the rejection frequency can be tuned from 3.8 GHz to 5.2 GHz, which corresponds to a 31% tuning range centered about 4.5 GHz. Note that no external DC bias was used and only 450 µW of optical power was required to achieve the maximum possible tuning. This is the lowest reported optical power [3-5] for bias-free optical control of a tunable filter. Note that the DC load resistance for this measurement was 500 KΩ, due to the parallel loading effect of the input and output probes (1 MΩ per probe). The performance of this circuit was also simulated on the HP EEsof linear test bench. The transmission line sections were modeled using the CPW element available in EEsof while actual measured s-parameter data was used for the OVC. The simulated results, shown in fig. (3.6b), are consistent with the measured data and the resonance frequency is off by less than 5.7 %. Note that the magnitude of the measured rejection is greater than 15 dB over all tuning states. Better rejection can be achieved by using multiple resonator sections, which is a straightforward extension of the circuit described here.

3.4 Optical control of a X-band analog phase shifter

Optical control of Schottky contacted CPW phase shifters has received considerable attention in the literature [6-8]. These phase shifters consist of a CPW line where the center conductor acts like a distributed Schottky contact while the ground planes serve as the ohmic contacts. The problem with these phase shifters is that the insertion loss is high and losses as high as 20 dB for a 180° phase shifter have been reported [7]. Also, these phase shifter circuits require a large reverse bias voltage to be applied across the Schottky diode. These problems have been overcome in the optically controlled phase shifter designed at UCSB. The phase shifter consists of a CPW line periodically loaded with shunt varactor diodes. The varactor diodes are controlled by an integrated photovoltaic array, which provides the bias for the circuit. The entire circuit including the CPW line, Schottky varactor diodes, PV array, RF-blocking resistor and the airbridges for connections are fabricated using the same process as the OVC. A picture of the optically controlled phase shifter circuit fabricated at UCSB is shown in fig. (3.7a). Note that this circuit differs from the conventional OVC circuits in that a single photovoltaic array simultaneously controls several varactor diodes. Since all the diodes in the phase shifter require the same reverse bias voltage, they can be controlled using the same PV array.

An equivalent circuit for the varactor-loaded CPW line controlled by the PV array is shown in fig. (3.7b). A high impedance transmission line (Z_0=77 Ω) is periodically loaded with varactor diodes (zero bias capacitance of 0.28 pF). When a uniform transmission line is periodically loaded, the structure exhibits Bragg frequencies at which the reflections add in phase and transmission through the structure is suppressed. For frequencies well below the lowest Bragg frequency, the periodic load elements can be absorbed into the line and the entire structure can be treated as an artificial transmission line with modified impedance and propagation characteristics. In the case of a CPW line loaded with varactor diodes, the capacitance per unit length of the artificial transmission line has contributions from the unloaded line capacitance (C_l) and the varactor capacitance (C_{var}). The inductance per unit length (L_l) of the artificial line is unchanged from that of the unloaded line. The characteristic impedance and phase velocity of the varactor diode loaded line are given by (3.1). Note that all terms involving the varactor capacitance are divided by the spacing between the diodes (L_{sect}) to obtain an equivalent varactor capacitance per unit length. It is evident from (3.1) that by varying the bias across the varactor diodes, it is

61

possible to change the varactor capacitance and hence the phase velocity. However changing the capacitance per unit length also changes the characteristic impedance of the artificial transmission line.
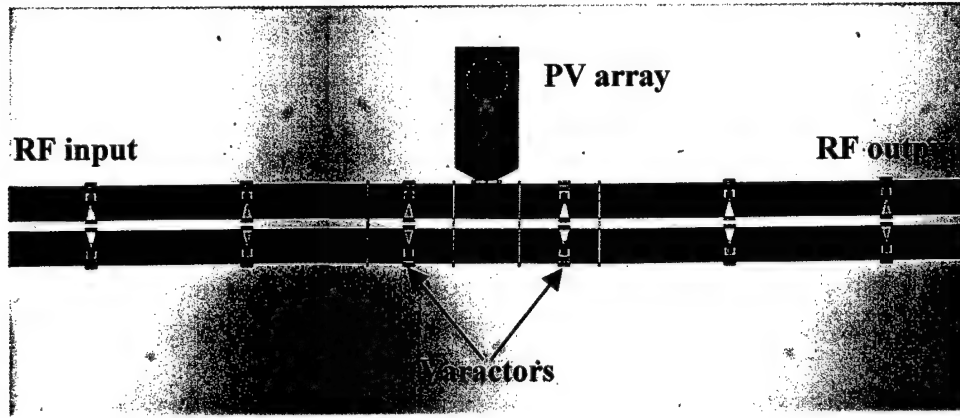

(a)
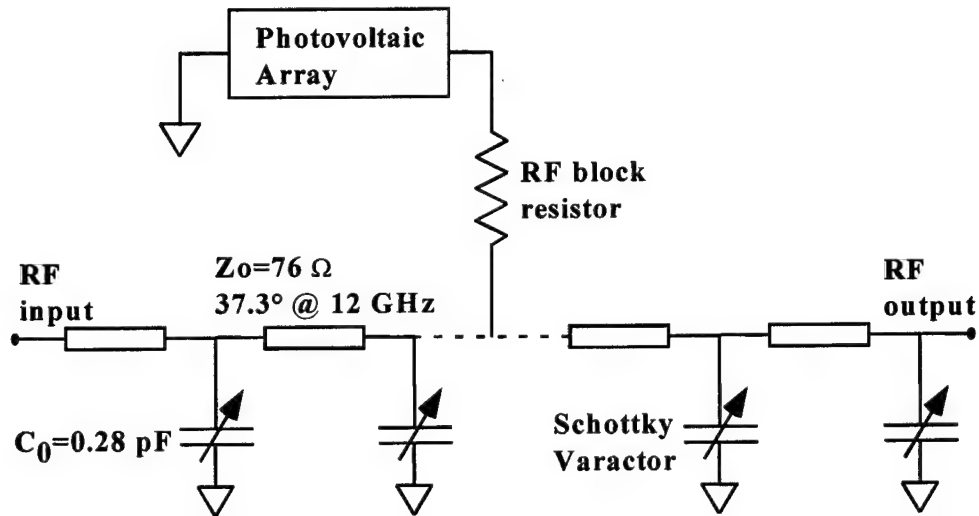
(b)

Figure 3.7: (a) Picture of an optically controlled phase shifter fabricated at UCSB (b) Equivalent circuit for the optically controlled phase shifter.

By reducing the variation in the total capacitance, the change in the characteristic impedance can be made small, at the cost of reducing the maximum change in propagation constant ($\Delta\beta^{max}$). However it is still possible to design the circuit for any desired maximum phase shift ($\Delta\phi^{max}$) by ensuring that the line is of suitable length (L_{total}) as given by (3.2).

$$Z_o(V) = \sqrt{\frac{L_t}{C_t + C_{var}(V)/L_{sect}}}$$ (3.1a)

$$v_{phase}(V) = \sqrt{\frac{1}{L_t(C_t + C_{var}(V)/L_{sect})}}$$ (3.1b)

$$\Delta\beta^{max} = 2\pi f \sqrt{L_t}\left(\sqrt{C_t + C_{var}^{max}/L_{sect}} - \sqrt{C_t + C_{var}^{min}/L_{sect}}\right)$$ (3.2a)

$$\Delta\phi^{max} = \Delta\beta^{max} L_{total}$$ (3.2b)

The phase shifter circuit fabricated at UCSB consisted of a CPW transmission line of characteristic impedance 77 Ω, periodically loaded with varactor diodes with zero bias capacitance of 280 fF. The periodic loading capacitors were implemented using two varactor diodes connected in parallel from the CPW center conductor to either ground plane in order to maintain the symmetry of the structure. The length of the unit cell (spacing between diodes) was chosen to be 980 μm resulting in a Bragg frequency of 18 GHz. 10 identical cells were connected in series to form an x-band analog phase shifter.

The measured differential phase shift as a function of frequency for different optical powers is plotted in fig. (3.8a). The measured insertion loss and return loss versus frequency curves for different illumination levels are shown in fig. (3.9a) and fig. (3.10a) respectively. From these curves it can be verified that the phase shifter circuit fabricated at UCSB is capable of 175° of phase shift at 12 GHz with less than 2.5 dB of insertion loss and return loss lower than −12 dB. The optical power required to achieve the maximum phase shift is only 450 μW. Moreover, no DC bias is required for the operation of the phase shifter. This is the best performance for a bias free optically controlled phase shifter [5, 7, 9].The microwave performance of the optically controlled phase shifter was also simulated on HP EEsof using the equivalent circuit model shown in fig. (3.7b). The simulated results for the differential phase shift versus frequency are shown in shown in fig. (3.8b) and show good agreement with the measured data. The simulation predicts a maximum phase shift of 180° at 12 GHz, which is only 2.8% higher than the measured phase shift of 175°. The simulated insertion loss versus frequency curves are depicted in fig. (3.9b) and maximum predicted insertion loss at 12 GHz is 2.3 dB which is only 0.15 dB lower than the measured insertion loss of the phase shifter. The simulated return loss curves are also similar to the measured data as shown in fig. (8.10b).

The performance of the optically controlled phase shifter rivals the performance of some of the best electronic phase shifters. This result shows the potential of the varactor diode loaded CPW line for microwave control applications.
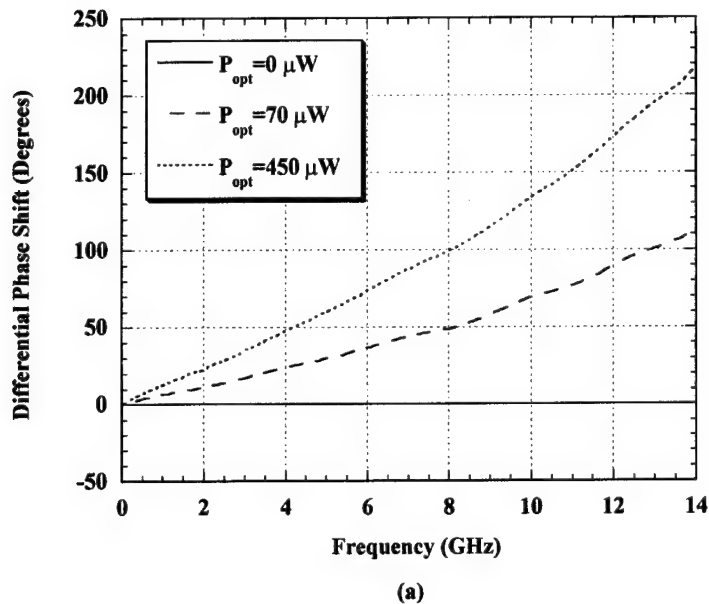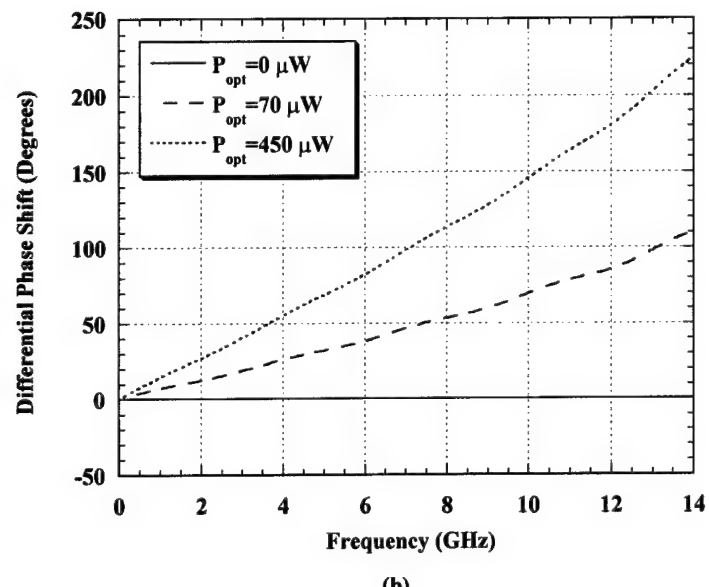
Figure 3.8: Differential phase shift versus frequency as a function of optical power- (a) measured data (b) simulated data
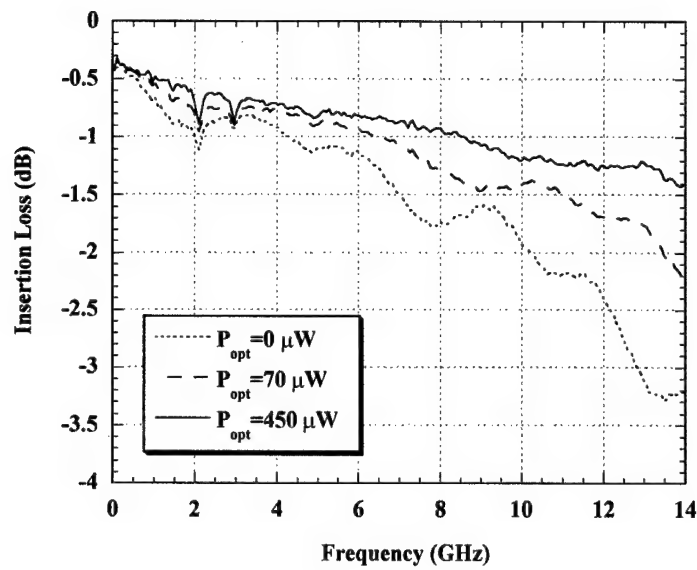
(a)
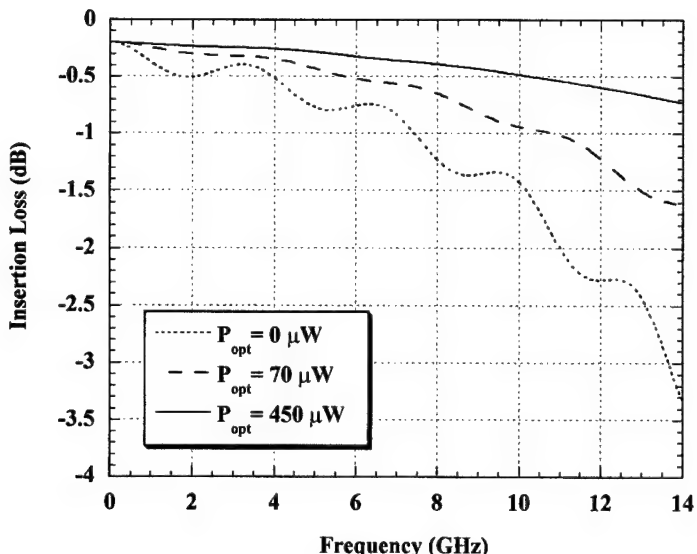
(b)

Figure 3.9: Measured (a) and simulated (b) insertion loss versus frequency data for different optical powers.
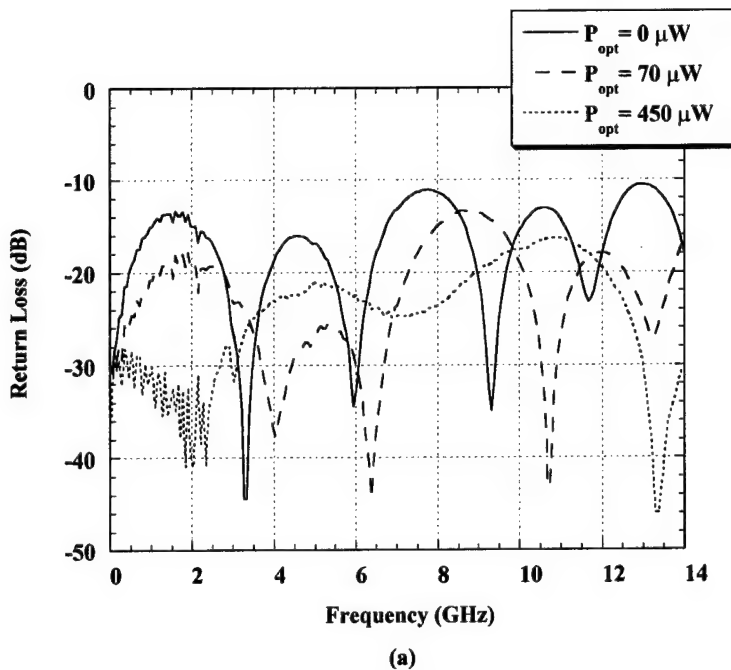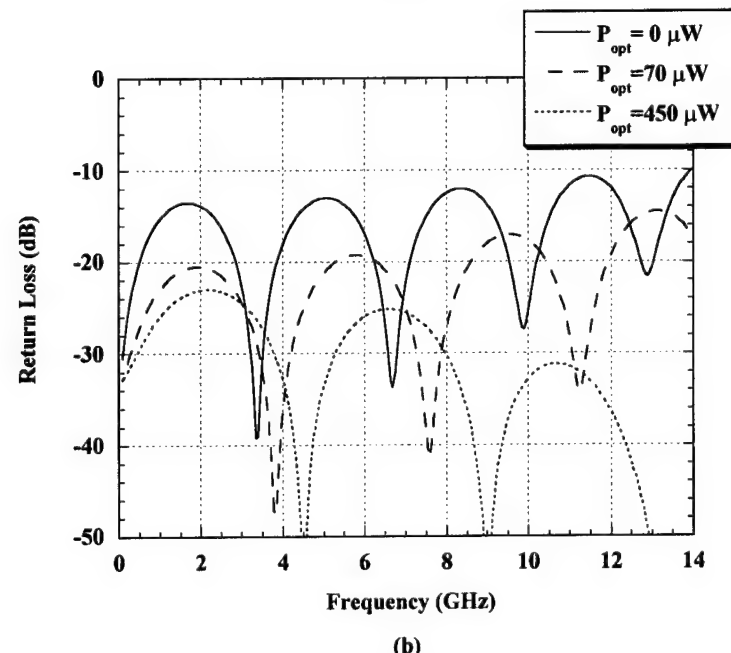
Figure 3.10: Measured (a) and simulated (b) return loss versus frequency curves for the optically controlled phase shifter.

3.5 Optical impedance tuning of a folded slot antenna

To demonstrate the usefulness of the OVC for controlling microwave antennas, an optically tunable slot antenna was designed, fabricated and tested at UCSB. Like the previously described circuits,

66

the optically tunable folded slot antenna was fabricated on GaAs and used the same fabrication process as the OVC. A picture of a folded slot antenna with an integrated OVC is shown in fig. (3.11a). The folded slot antenna was designed to be $\lambda/2$ long at 18 GHz. Due to capacitive loading of the antenna by the OVC the resonance frequency is shifted down to 14.5 GHz. When optical power is incident on the OVC, the capacitance decreases thus causing the resonance frequency to increase. Fig. (3.11b) shows that the folded slot resonance frequency can be tuned from 14.5 GHz to 16 GHz by using just 450 µW of optical power. This is the lowest reported optical power requirement for bias free control of a microwave antenna.
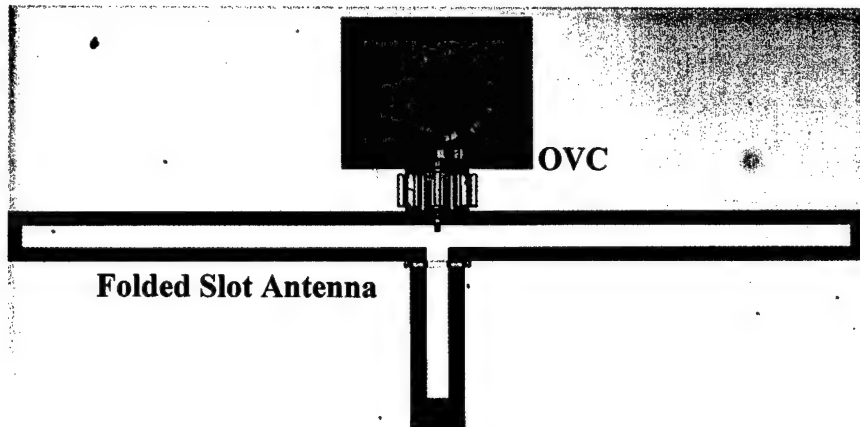

Figure 3.11: Picture of an optically tunable folded slot antenna fabricated at UCSB
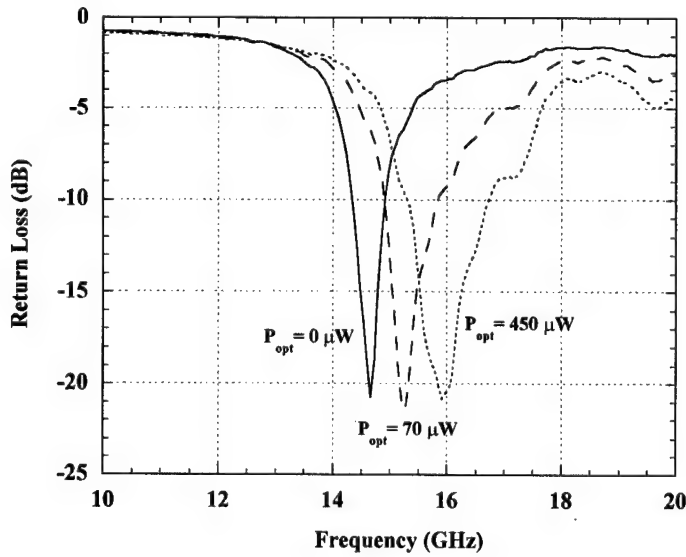

Figure 3.12: Measured return loss performance of an optically tunable folded slot antenna

67

3.6 Transient response of the OVC

Control components used in microwave circuits have response times that vary from milliseconds, for ferrite based devices, to nanoseconds for electronically controlled FETs/diodes. Photovoltaic control of FETs using hybrid PV arrays with rise and fall times of 2 μs and 20 μs respectively has been demonstrated. The response speed of the hybrid PV FET reported in [10] was limited by the large capacitance of the hybrid PV array. Since the monolithic OVC has a small PV array with lower junction capacitance, it is capable of faster response.

The transient response of the OVC was characterized using the setup shown in fig. (3.13a). A pulse generator with a 40 KHz square wave output was used to modulate the current output from the laser driver circuit. The laser driver circuit produced current pulses with rise and fall times of the order of 200 ns. Note that the laser driver circuit was not designed for rapid pulsed operation and hence tended to produce overshoot in the leading edge of the pulse. The light output from the 670 nm semiconductor laser diode followed the current waveform of the laser driver. The modulated light was input to the OVC using a 200 μm core diameter multi mode fiber. The voltage developed by the PV array across the OVC was used as the indicator of the OVC response. The OVC voltage was measured using Picoprobe SP11 active probes that were connected to a HP digitizing oscilloscope. The active probes, with a low input capacitance of 0.1 pF, were used to measure the array output voltage to avoid capacitive loading of the device under test by the measurement setup.

The rise and fall time of the OVC can be predicted using the simplified equivalent circuit models shown in fig. (3.13b,c). The model for the rise time consists of an ideal current source charging two capacitors in parallel. The amplitude of the current source is given by the photocurrent delivered by the PV array under short circuit conditions. $C_{array}(V)$ accounts for the depletion capacitance of the PV array while $C_{varactor}(V)$ accounts for the depletion capacitance of the Schottky varactor diode. Note that both the capacitors vary with the voltage across the OVC - the PV array capacitance tends to increase with voltage as the PV cells are getting forward biased while the Schottky varactor diode capacitance decreases since it is getting reverse biased. An exact solution for the rise time requires a numerical integration but an approximate value can be obtained from equation (3.3)

$$ t_r \approx \frac{C_{eff} V}{I_{sc}} \qquad (3.3) $$

where t_r is the rise time, V is the final voltage across the OVC under illumination, I_{sc} is the short circuit current generated by the PV array under illumination and C_{eff} is some effective capacitance to account for the two voltage variable capacitors. The simplified model for the fall time of the OVC is shown in fig. (3.13c) and consists of two capacitors discharging through a shunt load resistor. Note that the both the PV array capacitance as well as the Schottky varactor capacitance are voltage dependent and hence it is not possible to come with an analytical formula for the fall time. An approximate formula is given in (3.4)

$$ t_f \approx R_{load} C_{eff} \qquad (3.3) $$

where t_f is the fall time, R_{load} is the DC load resistance, and C_{eff} is some effective capacitance to account for the two voltage variable capacitors. Note that the effective capacitance used for the fall time calculation does not have to be the same as that used in the rise time calculations.

68
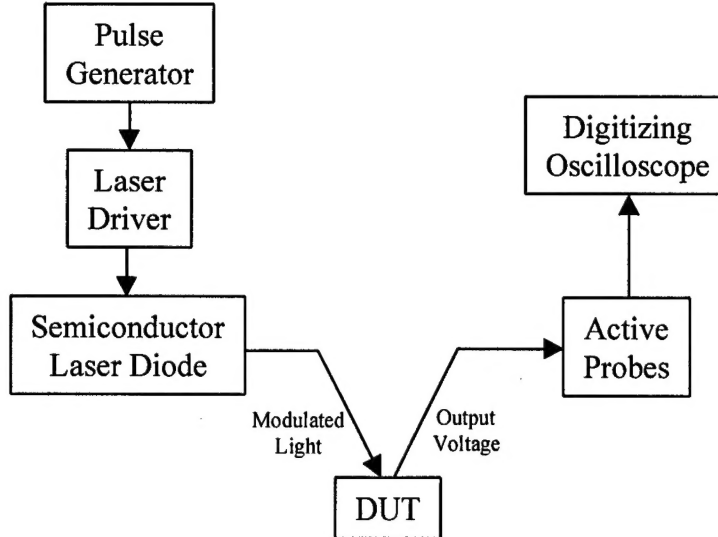
(a)
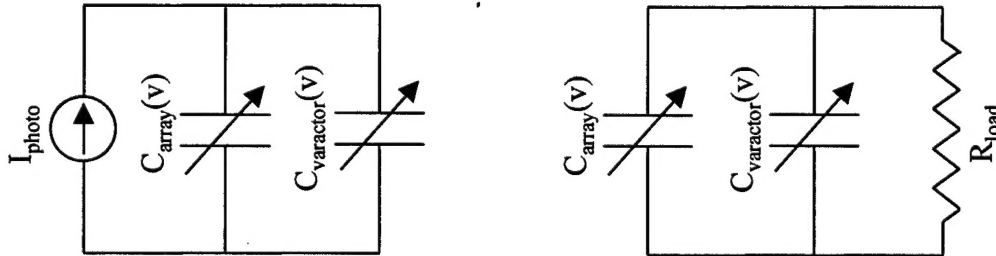
(b)   (c)

Figure 3.13: (a) measurement setup used for characterizing the transient response of the monolithic OVC. Simplified equivalent circuit models for the rise time (a) and fall time (b)

Although (3.3) and (3.4) can not be used to predict the exact rise and fall times, they can be used predicting the scaling laws. It is easily seen that decreasing the total capacitance of the OVC (includes both PV array and varactor capacitance) reduces both the rise and fall times. On the other hand, increasing the short circuit current by using more optical power only reduces the rise time. The DC load resistance helps reduce the fall time by providing a discharge path for the capacitors. In the absence of this load resistance, the capacitors discharge through internal leakage current which is very small, thus resulting in long fall times.

Some of these scaling laws have been tested by measurements and the results are presented in fig. (3.14a,b). Note that the overshoot at the leading edge is caused by the current overshoot in the laser driver circuit. Fig. (3.14a) depicts the effect of the zero bias capacitance on the response speed. Note that the rise time in both cases is very similar and is around 280 ns. This is because the rise time of the OVC is limited mainly by the rise time of the laser driver circuit, which is of the order of 200 ns. The fall time for the

69

circuit with zero bias capacitance of 1.4 pF is 4.1 μs while the fall time for the circuit with zero bias capacitance of 0.7 pF is 2.3 μs. Thus the fall time reduced by a factor of 1.8 when the zero bias capacitance was decreased by a factor of 2. Note that the peak optical power for these measurements was 600 μW and the DC load resistance was 1 MΩ.
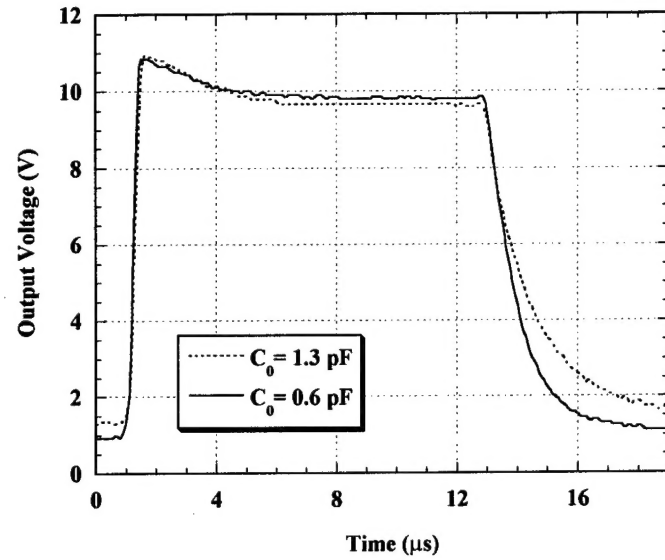
(a)
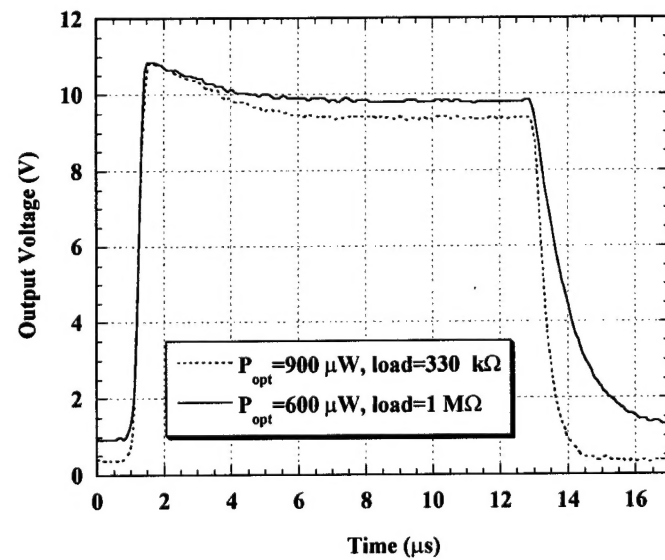
(b)

Figure 3.14: (a) Effect of total OVC zero bias capacitance on the switching speed (b) effect of DC load resistance on the switching speed of the OVC

The effect of the DC load resistance on the fall times is depicted in fig. (3.14b) and shows that when the load resistance was reduced from 1MΩ to 330 KΩ, the fall time decreased from 2.3 pF to 780 ns (almost a factor of 3). The rise time was again limited mainly by response speed of the laser driver circuit and was similar for both cases. Note that when the DC load resistance was reduced to 330 KΩ, the peak optical power had to be increased to 900 µW to maintain the same peak output voltage. This is to be expected based on the results from the last section where it was shown that smaller loads require higher optical powers to achieve the same PV array output voltage.

Zero bias capacitance	DC load resistance	Rise Time	Fall Time
1.4 pF	1 MΩ	290 ns	4.1 µs
0.7 pF	1 MΩ	270 ns	2.3 µs
0.7 pF	330 KΩ	290 ns	780 ns

Table 3.1: Summary of the measured rise and fall times of the OVC

A summary of the rise and fall times is presented in table (3.1). The rise time for the arrays is of the order of 280 ns and is measurement setup limited. The fall time is a strong function of the zero bias capacitance and the DC load resistance and can be made as small as 780 ns. These response times are adequate for most microwave control applications.

References

[1]   S. T. Allen, U. Bhattacharya, and M. J. W. Rodwell, "Multi-terahertz sidewall-etched varactor diodes and their application in submillimetre-wave sampling circuits," *Electronics Letters*, vol. 29, pp. 2227-8, Dec. 1993.

[2]   S. T. Allen, "Schottky Diode Integrated Circuits for Sub-Millimeter-Wave Applications," *Ph.D. Thesis*: University of California at Santa Barbara, 1994.

[3]   Y. Yamamoto, K. Kawasaki, and T. Itoh, "Optical control of microwave active band-pass filter using MESFETs," in *1991 IEEE MTT-S International Microwave Symposium Digest 91CH2870-4*, Boston, MA, USA, 1991, , pp. 655-8.

[4]   H. Hayashi, M. Nakatsugawa, T. Nakagawa, and M. Muraguchi, "A novel optical control technique using tunable inductance circuits," *IEICE Transactions on Electronics*, vol. E81-C, pp. 299-304, Feb. 1998.

[5]   A. S. Nagra, O. Jerphagnon, P. C. Chavarkar, M. L. VanBlaricum, and R. A. York, "Indirect control of Microwave circuits using low optical power," *IEEE Transactions on Microwave Theory and Techniques*1999.

[6]   P. Cheung, D. P. Neikirk, and T. Itoh, "Schottky-biased, optically controlled coplanar waveguide phase-shifter," *Electronics Letters*, vol. 25, pp. 1301-2, Sept. 1989.

[7]   P. Cheung, D. P. Neikirk, and T. Itoh, "Optically controlled coplanar waveguide phase shifters," *IEEE Transactions on Microwave Theory and Techniques*, vol. 38, pp. 586-95, May. 1990.

[8]   Y. D. Lin, D. P. Neikirk, and T. Itoh, "Coplanar waveguide phase shifter controlled by a spatially periodic optical illumination," *International Journal of Infrared and Millimeter Waves*, vol. 8, pp. 1027-36, Sept. 1987.

[9]   S. J. Rossek and C. E. Free, "Optically controlled microwave switching and phase shifting using GaAs FET's," *IEEE Microwave and Guided Wave Letters*, vol. 5, pp. 81-3, March. 1995.

[10]   C. K. Sun, R. Nguyen, C. T. Chang, and D. J. Albares, "Photovoltaic-FET for optoelectronic RF/ mu wave switching," *IEEE Transactions on Microwave Theory and Techniques*, vol. 44, pp. 1747-50, Oct. 1996.